

Optical properties of boreal forest fire smoke derived from Sun photometry

N. T. O'Neill,¹ T. F. Eck,² B. N. Holben,³ A. Smirnov,² A. Royer,¹ and Z. Li^{4,5}

Received 25 May 2001; accepted 13 November 2001; published 13 June 2002.

[1] Aerosol optical properties derived from Sun photometry were investigated in terms of climatological trends at two Sun photometer sites significantly affected by western Canadian boreal forest fire smoke and in terms of a 2-week series of smoke events observed at stations near and distant from boreal forest fires. Aerosol optical depth (τ_a) statistics for Waskesiu, Saskatchewan, and Thompson, Manitoba, were analyzed for summer data acquired between 1994 and 1999. A significant correlation between the geometric mean and the forest fire frequency indices (hot spots) was found; on the average, 80% of summertime optical depth variation in western Canada can be linked to forest fire sources. The average geometric mean and geometric standard deviation at 500 nm was observed to be 0.074 and 1.7 for the clearest, relatively smoke-free summer and 0.23 and 3.0 for the summer most influenced by smoke. A systematic decrease of fine mode Angstrom exponent (α_f) was noted ($d\alpha_f/d \log \tau_a \sim -0.6$). This decrease roughly corresponds to an increase in the fine mode effective radius (r_{eff}) from 0.09 to 0.15 μm and an abundance (A) to size rate increase near 2.0 ($d \log A / d \log r_{\text{eff}}$). A 1998 series of forest fire events was tracked using TOMS, AVHRR, and GOES imagery, back trajectories, and data from six Sun photometer sites in Canada and eastern United States. The results showed rates of decrease of α_f with increasing τ_a which were similar to the climatological data. An analysis in terms of source to station distance showed a decrease in α_f and an increase in r_{eff} with increasing distance. This observation was coherent with previous observations on the particle growth effects of aging. **INDEX TERMS:** 0360 Atmospheric Composition and Structure: Transmission and scattering of radiation; 0305 Atmospheric Composition and Structure: Aerosols and particles (0345, 4801); 3360 Meteorology and Atmospheric Dynamics: Remote sensing; 4801 Oceanography: Biological and Chemical: Aerosols (0305); **KEYWORDS:** aerosols, forest fire smoke, Sun photometry, optics

1. Introduction

[2] Smoke particulates associated with biomass burning represent an important aerosol whose global rate of production is comparable to that of sulfate aerosols [Radke, 1989; Houghton *et al.*, 2001]. The influence of smoke in terms of direct and indirect radiative forcing, air pollution, atmospheric chemistry, and visibility reduction is significant both at local and regional scales [Kaufman *et al.*, 1998; Woods *et al.*, 1991; Li, 1998]. Smoke emissions are readily observed by satellite sensors and as such serve as a means of monitoring the long-range transport of smoke aerosols as well as providing remotely sensed indicators of particulate emission rates and the emission rates of associated trace

gases [Ward *et al.*, 1991]. Ground-based and airborne observations of smoke are needed to support and validate satellite-monitoring programs and to provide data that cannot be obtained from satellite inversions. The development of databases and climatological parameterizations from all observation techniques is important in order to better understand and model the behavior of these aerosols.

[3] Boreal forest fires within Canada consume an area that is about 40% of the area consumed by all boreal forest fires [Stocks, 1991]. In terms of a global biomass burning budget, boreal forest fires account for less than 10% (even in peak burning season) of worldwide biomass burning activity [Dwyer *et al.*, 1998]. In spite of these modest global contributions the effect of smoke generated by western Canadian forest fires as a nonindustrial source of pollution and in terms of general visibility considerations is significant not only in western Canada [Chung, 1984] and the Canadian Arctic [Hariss *et al.*, 1992] but also in eastern North America [Westphal and Toon, 1991]. Observations in the latter case are not confined to optical smoke monitoring; Wotawa and Trainer [2000] observed that the major source of CO variation over a 2-week period at four eastern U.S. stations was large forest fires in northwestern Canada, while Robock [1988] demonstra-

¹CARTEL, Université de Sherbrooke, Sherbrooke, Quebec, Canada.

²Goddard Earth Sciences and Technology Center, University of Maryland-Baltimore County, Baltimore, Maryland, USA.

³NASA Goddard Space Flight Center, Greenbelt, Maryland, USA.

⁴Canada Centre for Remote Sensing, Ottawa, Ontario, Canada.

⁵Now at Department of Meteorology, University of Maryland, College Park, Maryland, USA.

ted significant short-term reductions in surface temperature over North America induced by an extended smoke plume originating in British Columbia.

[4] A considerable body of research using in situ sampling techniques has been published on the microphysical and optical properties of smoke. This includes the analysis of laboratory burns [Patterson and McMahon, 1984; Hallett *et al.*, 1989], airborne monitoring of prescribed or local forest fires [Radke *et al.*, 1978, 1988; Pueschel *et al.*, 1988; Hallett *et al.*, 1989; Pueschel and Livingston, 1990; Hobbs *et al.*, 1996], and intensive field campaigns involving large-scale forest fires in the Amazon region [Reid and Hobbs, 1998; Reid *et al.*, 1998; Echalar *et al.*, 1998]. Remote sensing techniques have included ground-based Sun photometry [Kaufman *et al.*, 1992], enhanced satellite imagery [Chung, 1984; Li *et al.*, 2001], quantitative inversions of satellite imagery for smoke optical parameters [Ferrare *et al.*, 1990; Hsu *et al.*, 1999; Li and Kou, 1998b; Zhang *et al.*, 2001; Wong and Li, 2002], and ground-based lidar combined with solar occultation satellite instruments [Fromm *et al.*, 2000].

[5] The use of ground-based Sun photometry provides optical indicators of smoke properties which, although crude in the absence of any vertical discrimination capabilities, are robust, nonintrusive, and instantaneous measures of column-integrated aerosol properties. Such measurements are important sources of validation for satellite retrieval algorithms as well as for climatological to meteorological scale aerosol dynamics models. Satellite inversions suffer from signal competition due to surface-reflected photons, while aerosol models require stable benchmark indicators to validate their aerosol transport and chemical algorithms.

[6] Little research on the use of Sun photometry to characterize smoke was published until the deployment of the AERONET network in the early 1990s. Sun photometry work of this nature has, however, been almost exclusively focused on Amazonian tropical forest fires and African savannah fires [Kaufman *et al.*, 1992; Holben *et al.*, 1996; Remer *et al.*, 1998; Dubovik *et al.*, 1998; Eck *et al.*, 1999; Holben *et al.*, 2001; Eck *et al.*, 2001]. A relatively small body of literature exists concerning smoke parameter measurements linked to western or central Canadian forest fire sources. Some in situ airborne measurements have been reported [Pueschel *et al.*, 1988; Radke *et al.*, 1991; Mazurek *et al.*, 1991; Miller and O'Neill, 1997] as well as particulate sampling measurements during smoke events [Chung, 1984]. Significant numbers of observations using satellite data have been reported, usually in the context of tracing smoke plume evolution over the urbanized areas of eastern North America [Chung and Le, 1984; Westphal and Toon, 1991; Ferrare *et al.*, 1990; Hsu *et al.*, 1999; Fromm *et al.*, 2000; Li *et al.*, 2001]. Sun photometry of Canadian or American forest fire smoke is largely limited to short experiments [Pueschel *et al.*, 1988; Pueschel and Livingston, 1990] or generalized studies that were not limited to smoke events and which did not attempt to discriminate smoke effects from other aerosol effects [Markham *et al.*, 1997]. The exception is the multiannual analysis of Thompson, Manitoba, data in the Sun photometer climatological analysis of Holben *et al.* [2001].

[7] This paper is an attempt to explicitly link Sun photometry measurements with indicators of the influence of forest fire smoke from the Canadian west. It is divided into two major parts; multiyear Sun photometry data from two long-term sites whose aerosol variation is clearly affected by forest fire smoke is presented in section 3, while section 4 is dedicated to the study of a series of forest-fire-induced smoke events which occurred in the first two weeks of August 1998. The attendant objectives are (1) to infer climatological optical statistics of smoke and to analyze the link between optical depth variance and forest fire smoke from western Canada and (2) to record and optically characterize individual cases of large optical depth variations which are known to be induced by western Canadian boreal forest fire smoke and which were measured at various distances from the sources. The latter data are viewed as a means of providing an independent smoke optical depth reference to the optical climatological inferences.

2. Methodological Considerations

2.1. Optical Analysis Techniques

2.1.1. Definition of standard optical parameters

[8] Five standard optical parameters, all extracted from the spectral Sun photometer data, were employed to derive the results presented in this paper. They are the aerosol optical depth (τ_a), the Angstrom exponent (α), the spectral derivative of the Angstrom exponent ($\alpha' = d\alpha/d \ln \lambda$), the fine mode Angstrom exponent (α_f), and the ratio (η) of the fine mode optical depth (τ_f) to τ_a . These parameters are all evaluated at the reference wavelength of 500 nm after having passed a third-order polynomial of $\ln \tau_a$ versus $\ln \lambda$ through each data spectrum [O'Neill *et al.*, 2001b].

[9] The Angstrom exponent is a standard optical analysis parameter which is related to particle size and, to a lesser degree, refractive index. Aerosol optics are largely dominated by a particle size distribution which can be subdivided into a submicron accumulation (fine) mode and a supermicron coarse mode. Given this simple distribution partitioning, one can easily show that α and α' are expressible in terms of analogous fine and coarse mode exponents weighted by η [ibidem];

$$\alpha = \alpha_f \eta + \alpha_c (1 - \eta), \quad (1a)$$

$$\alpha = \alpha'_f \eta + \alpha'_c [1 - \eta] - \eta [1 - \eta] (\alpha_f - \alpha_c)^2. \quad (1b)$$

[10] The derivative α' indicates spectral curvature of α at $\lambda = 500$ nm and is itself sensitive to particle size and refractive index. Eck *et al.* [2001] demonstrated distinct differences in this parameter for lightly absorbing urban aerosols versus smaller, more highly absorbing biomass burning aerosols. Given certain a priori information concerning the optical behavior of the coarse particle mode and α'_f , equations (1a) and (1b) can be inverted to yield α_f and the optical fraction $\eta = \tau_f/\tau_a$ [O'Neill *et al.*, 2001a].

2.1.2. Dependency of α_f on r_{eff} and on τ_a

[11] The fine mode Angstrom exponent can be shown to be a nearly monotonic function of the effective particle radius (r_{eff}) (see O'Neill and Royer [1993] and Shifrin [1995], for example, and see the Notation section for a definition of r_{eff}). Figure 1a shows a plot of α_f versus r_{eff} for a Mie simulation of east coast North American aerosols

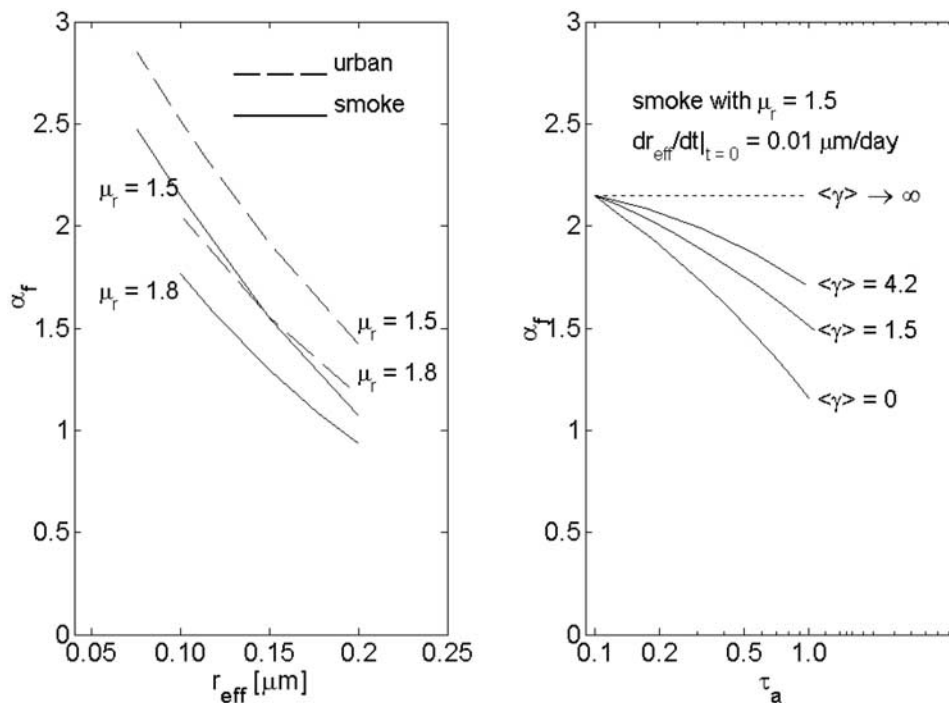


Figure 1. (a) Mie simulations of α_f versus r_{eff} for continental and smoke-like lognormal distributions at a wavelength of 500 nm (μ_r refers to the geometric standard deviation of the lognormal size distribution). The smoke aerosol was modeled as an inner carbon core of refractive index (m) = $1.8 - 0.6i$ and an outer shell with $m = 1.5 - 0i$. The carbon core occupied a volume of 6% of the total [Reid *et al.*, 1999]. A change to 12% volumetric fraction produced curves that were less than 15% below the 6% curves. The continental aerosol was a homogeneous sphere ($m = 1.43 - 0.0035i$ as per Remer *et al.* [1999]). (b) α_f versus τ_a for the $\mu_r = 1.5$, smoke case of Figure 1a and different rates of average abundance increase ($\langle\gamma\rangle = d \log A/d \log r_{\text{eff}}$; see Appendix B for details).

[Remer *et al.*, 1999] and biomass burning aerosols [Reid *et al.*, 1999]. Although there are differences in the fine mode Angstrom exponent between the different aerosol models, significant information about r_{eff} can clearly be extracted from a knowledge of α_f even in the absence of any a priori information on the type of aerosol being measured.

[12] The dependence of α_f on τ_a can be expressed analytically (compare Appendix B). Figure 1b shows computations applied to a subset of the Mie simulations of Figure 1a for an illustrative example (in this particular example we imagined an influx of particles whose rate of change of effective radius was proportional to the abundance ($dr_{\text{eff}}/dt = KA$) and that the abundance was in turn linearly dependent on time ($dA/dt = \text{constant}$); in such a case, γ , the rate of relative increase of abundance to r_{eff} , is equal to $[dA/dt \times r_{\text{eff}}]/[KA^2]$). The slopes of these curves are dependent on the mechanism which increases τ_a ; the decrease in α_f for the steepest slope of Figure 1b is due to a pure increase in particle size, while the progressively smaller slopes are due to the ever increasing contributions of aerosol particle number. The magnitude of the rates of increase of r_{eff} , which were employed to produce this figure, was inspired by typical rates for aged smoke [Reid *et al.*, 1998]. For the three nonzero slope examples, a regression through the curves of Figure 1b from $\tau_a = 0.1$ to $\tau_a = 1.0$ yielded values of $d\alpha_f/d \log \tau_a = -0.99$, -0.64 , and -0.45 . These values correspond to (average) abundance to particle size change rates of 0.0, 1.5, and 4.2 (the average of the parameter $\gamma = d \log A/d \log r_{\text{eff}}$ defined

in Appendix B). At a more approximate but generalized level, equation (B5) of Appendix B permits an order of magnitude estimate of $\langle\gamma\rangle$ given values of $d\alpha_f/d \log \tau_a$.

2.2. Sun Photometer Data

[13] The optical data employed throughout this work were extracted from the automated CIMEL Sun photometer/sky radiometers belonging to the AERONET and/or AEROCAN network (the AEROCAN network is a Canadian subnetwork of AERONET). In solar extinction mode the CIMEL operates in seven spectral bands (340, 380, 440, 500, 675, 870, and 1020 nm plus a 940 nm water vapor band), and in sky radiance mode, it scans off the solar disk to acquire sky radiance data at four wavelengths (440, 500, 675, and 1020 nm). Details concerning the operations and data processing logistics of this network are given by Holben *et al.* [1998].

[14] In this work we largely limited ourselves to the extinction mode data and excluded the 340 nm band from the seven bands given above since this band is typically more susceptible to errors than the other bands. Formal inversions of extinction and sky radiance were available [Dubovik and King, 2000] but represent a different, much smaller data set. Although some of the inversion data are presented below, we concentrated on the more conventional extinction data given its more robust statistical weight and given that any aerosol content and (average) size trends can be monitored from the purely optical parameters. These

parameters also have the added advantage of being more easily comparable with other observations.

[15] The first step in our analysis technique was to visualize the five standard optical parameters as a set of four graphs with τ_a being the dependent variable for α , α' , α_f , and η , respectively (compare Figure 4). This type of representation is an extension of the traditional α versus τ_a graph wherein particle type and particle number information are presented simultaneously as a two-dimensional histogram in order to facilitate discrimination between different classes of particles [e.g., Kaufman and Fraser, 1983]. An intensive analysis of these quartets of graphs then led to the production of summary trend statistics, which we present in this paper.

[16] In Appendix A we give details on the weighting scheme used to quantify confidence levels in α , α' , α_f , and η . Because most work on the Angstrom exponent is based on a (classical) multiwavelength exponent derived from a spectral regression, we also derive an empirical relation between our monochromatic exponent and the classical exponent.

3. Climatological Optical Data in Western Canada

[17] General Sun photometry measurements without a specific focus on smoke aerosols have been carried out in Canada over a period that extends at least from the initial deployment of the BAPMoN network Sun photometers in the early 1970s [Forgan *et al.*, 1993]. A number of papers whose objective was to characterize the general climatological behavior of the aerosol optical depth and often the Angstrom coefficient were written in subsequent years [Gueymard, 1994; Smirnov *et al.*, 1994, 1996; Markham *et al.*, 1997; Fedosejevs *et al.*, 2000]. Mention should also be made of the much longer climatological records obtained from turbidity (panchromatic) data [Yamashita, 1974; Polavarapu, 1978; Freund, 1983; Uboegbulam and Davies, 1983; Gueymard and Garrison, 1998].

3.1. Links Between Forest Fire Smoke and Aerosol Optical Depths

[18] Holben *et al.* [2001] reported on the general aerosol optical depth statistics of the AERONET site at Thompson, Manitoba, and qualitatively linked this behavior to forest fire activity. This site is on the northern edge of the boreal forest zone and is regularly affected by smoke plumes of western Canadian forest fires during the fire season. Holben's multiyear statistics showed substantial variation of the aerosol optical depth which they attributed mostly to forest fire smoke. The basis for this observation was the multiyear TOMS estimates of smoke coverage [Hsu *et al.*, 1999] and a general knowledge of the predominant aerosol influences. Li *et al.* [1997] made a similar observation from qualitative comparisons of Sun photometer data and the known presence of smoke observed in AVHRR imagery.

[19] Figure 2a is a plot of total hot spot counts for all of western Canada as detected using AVHRR thermal imagery [Li *et al.*, 2001]. Hot spot count is closely related to the more relevant parameter of area burned [Fraser *et al.*, 2000]. Figures 2b and 2c are plots of the geometric mean ($\tau_{a,g}$) and geometric standard deviation (μ_τ) [O'Neill *et al.*, 2000] of the aerosol optical depth at 500 nm computed for summer ensembles of data (June, July, and August) at the Thompson,

Manitoba, site and a second site at Waskesiu, Saskatchewan, from 1994 to 1999 (details on the lognormal distribution are given by O'Neill *et al.* [2000]). In spite of the spatial disparity in comparing a regional variable with essentially point variables the level of correlation between hot spot counts and $\tau_{a,g}$ (or μ_τ) is significant or close to significant at the 0.05 confidence level. In particular, one can observe the large values of $\tau_{a,g}$ and μ_τ in the active fire years of 1994 and 1995 and the correspondingly low values in the relatively fire-free (wet) year of 1997. The corresponding correlation coefficients (R) between $\tau_{a,g}$ and the hot spot count over all years were 0.69 and 0.85 for Thompson and Waskesiu, respectively, while the analogous coefficients for the geometric standard deviation μ_τ were 0.91 and 0.65. Such correlations provide independent if circumstantial support of the observations of Holben *et al.* [2001] concerning the dominance of biomass burning aerosols on the optical depth variation observed at Thompson.

[20] The 1997 case serves as benchmark from which one can estimate the background statistics of optical depths for aerosols other than smoke during our nominal 3-month summer period of June, July, and August. The values of $\tau_{a,g}$ and μ_τ were 0.08 and 1.6 and 0.07 and 1.8 for Waskesiu and Thompson, respectively. The modal values of 0.055 and 0.056 (peak of a lognormal fit on a linear τ_a axis) are lower than the value of 0.087 estimated from a lognormal fit to the summer data of Smirnov *et al.* [1996] for Wynyard, Saskatchewan. If, however, one applies their synoptical air mass theory and their all-season, synoptical air-mass-dependent histograms to estimate a weighted modal average (based on the frequency of occurrence of different synoptical air masses during the summer) then the value obtained is 0.067.

[21] Further to the generic approach represented by Figure 2, a sectorial correlation analysis was performed for each summer period of each year to determine which sector or sectors provided the best correlation coefficient with $\tau_{a,g}$. In this case the regression space consisted of the nine temporal bins (of 10-day composite data) stretching across the June, July, and August summer period. R values were computed for all 63 possible hot spot combinations of six individual sectors: Saskatchewan, Manitoba, the Northwest Territories, Alberta, Yukon, and Nunavut (British Columbia was excluded to simplify the computations and because it never contributed more than 3.5% of the total number of hot spots in any given year). Figure 3 shows the six sectors as well as the two key Sun photometer sites of Thompson and Waskesiu. The hot spot distribution for 1998 is overlain on this map to illustrate the type of geographical dispersion one obtains for a given year.

[22] Table 1 shows the highest R values in any given year along with the combination of sectors which yielded the highest correlation. Often, the difference in R was not very sensitive to the addition or exclusion of source sectors to certain fundamental sectors, and the simplest source combination was chosen when differences were less than 0.01. It can be observed that the R values are all greater than 0.7, with the exception of Waskesiu during the clear 1997 background year. It should be noted that Nunavut sources of 1994 represent a questionable result, given the relatively small number of hot spots and because R was a fairly isolated value (the next highest value of R was 0.601 for 14,906 hot spots associated with Saskatchewan, Manitoba,

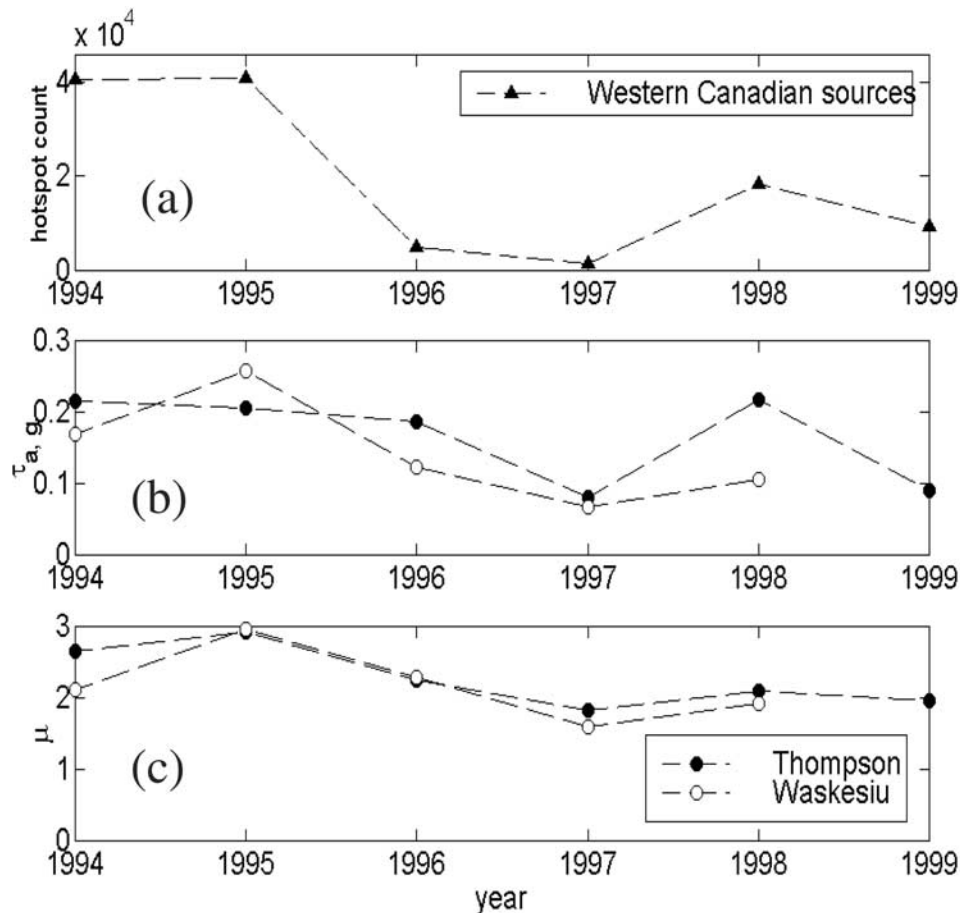


Figure 2. (a) Hot spot count for western Canada versus year. (b, c) Geometric mean and geometric standard deviation of $\tau_{a,g}$ for the Thompson and Waskesiu sites versus year. The averaging period is the summer months of June, July, and August ($\lambda = 500$ nm; optical data are cloud screened and error weighted).

and Nunavut). On the whole, these systematic results clearly imply a significant association between forest fire sources and variations in $\tau_{a,g}$; for both stations and all years, an average of 80% of the 10-day composite variation in $\tau_{a,g}$ can be linked with hot spot activity.

3.2. Trends in Angstrom Exponents

[23] Figure 4 shows an example of the standard optical parameter graphs for 1996. The error bars are indicators of weighted data variance (see Appendix A), while the number of samples/bin which contributed to the computation of the weighted means and variances are indicated in the bottom left-hand graph of each quartet. These quartets of graphs were computed for all sites and all years and served as an intermediate analysis tool from which regression statistics versus τ_a were derived and analyzed. It was found that these results were fairly robust and would survive, for example, a change from third to second order of the polynomial fit, which was applied to all $\ln \tau_a$ spectra.

[24] The data of 1996 were unique in that a histogram of α values showed an extreme case of bimodality that was suggestive of a strong influence of thin cloud (one of the α modes was near zero). The cloud-induced mode is the cause of the rapid decrease of α and η with increasing τ_a as well

as the large variances at large τ_a . It should be emphasized that the cloud-screening algorithm does not guarantee cloud elimination since the criterion employed for optical depth elimination is largely based on temporal excursions in magnitude and not on spectral dependency. *Smirnov et al.* [2000b] purposely did not include spectral dependency as a cloud flag criterion in order to minimize the possible exclusion of legitimate large-particle optical depths such as those due to dust events. Spatially homogeneous thin cloud events can thus survive the cloud-screening process.

[25] Figure 5, which shows yearly summer averages of α_f and α for both Waskesiu and Thompson at large τ_a (unity), demonstrates the consistency of the α_f estimate; the low values of the α averages observable in 1996 and 1997 are most likely the result of (spatially homogeneous) thin cloud contamination, while the relatively stable values of α_f suggest that the cloud contamination is largely filtered out.

[26] Figure 6 illustrates the systematic nature of the decrease in α_f with increasing τ_a which was observed for nearly all years. On average, for both sites, the decrease between $\tau_a = 0.1$ and $\tau_a = 1.0$ corresponds to a α_f change from about 2.2 to 1.6 ($d\alpha_f/d \log \tau_a \sim -0.6$) or hence a value of $\langle \gamma \rangle$ near 2 ($\langle d \log A / dr_{\text{eff}} \rangle$ of equation (B5)). From the variation

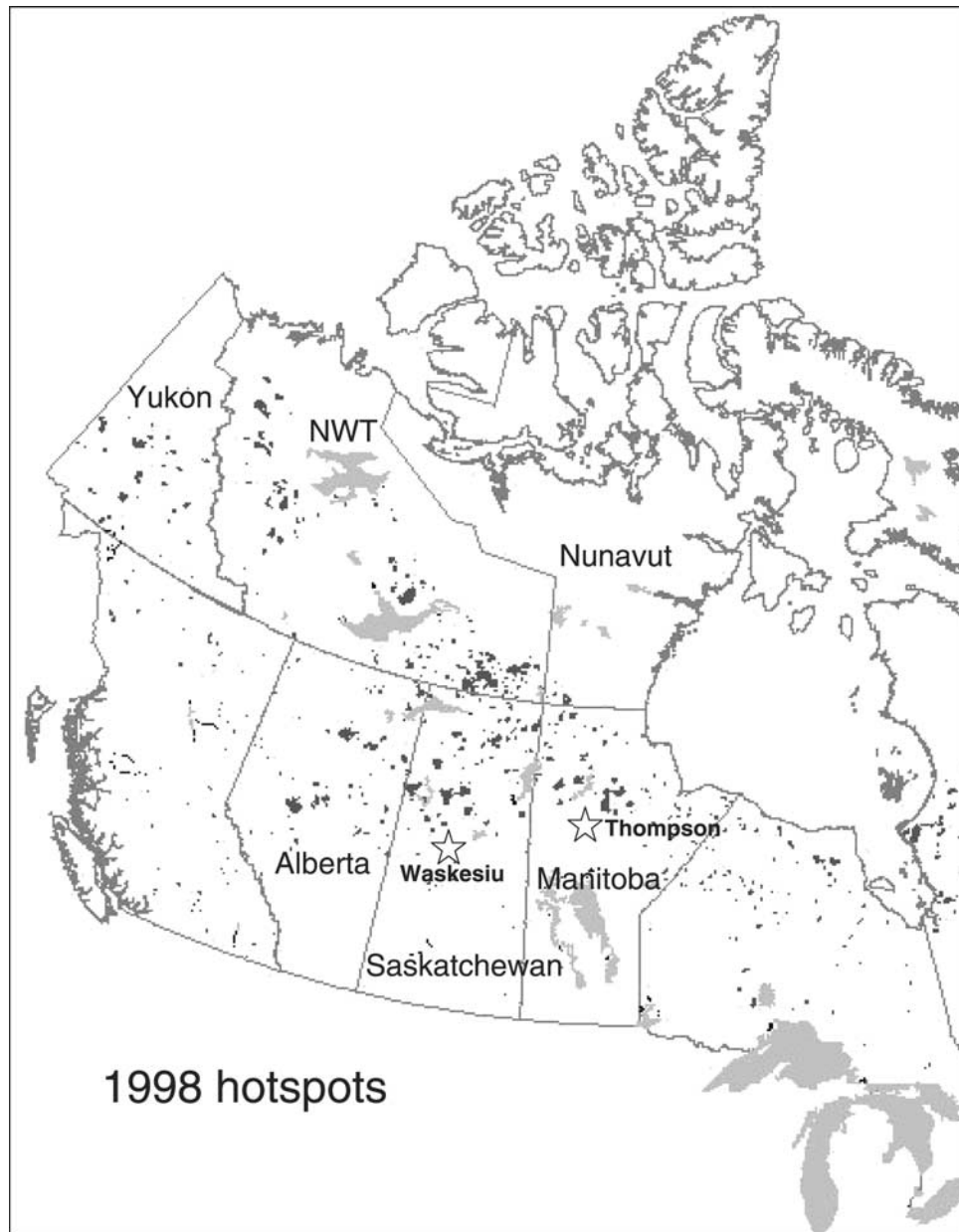


Figure 3. Map of western Canada showing the six sectors and the Thompson and Waskesiu Sun photometer sites. The hot spots for the 1998 burning season (dark grey points) are overlain to illustrate the appearance of a typical hot spot distribution. The hot spot counts for these six regions were used to generate Table 1.

of all the curves of Figure 1a, this change in α_f corresponds to a rough increase in r_{eff} from about 0.09 to 0.15 μm (where the uncertainty associated with the range of all the curves is about $\pm 0.03 \mu\text{m}$). The significant exception to this trend is clearly Thompson 1998, where both α and α_f were practically constant and equal across all values of τ_a (η was always near unity). This trend was found to be very robust (reasonably independent of changes in spectral polynomial order and omitted wavelengths, for example) and thus appears to be significant. It would correspond to conditions dominated by fine mode optics where changes in optical depth are for the most part due to changes in particle number rather than particle size. Table 2 summarizes the trends of both α and α_f versus τ_a in terms of three parameters which result from a linear-log fit to the weighted data (typified by Figure 4). With

the notable exception of Thompson 1998, the slope parameter ($a = d\alpha_f/d\log \tau_a$) is typically more negative for heavy smoke years (1994 and 1995) than for low-turbidity years (1997).

[27] This type of α_f decrease is consistent with the findings of Reid *et al.* [1999] for Brazilian forest fires and those of Eck *et al.* [2001], who indicated a tendency toward increasing accumulation mode particle size with increasing τ_a for African biomass burning aerosols. Similar trends have also been observed for more continental accumulation mode aerosols [O'Neill *et al.*, 2001b]. The use of an Angstrom exponent constrained to short wavelengths in the two former papers yields an exponent that is similar to the fine mode Angstrom exponent employed in the present work since the fine mode optical depth increases in relative importance with decreasing wavelength ($\eta \rightarrow 1$).

Table 1. Highest Correlations Between $\tau_{a,g}$ and Hot Spot Count From the Set of 63 Source Sector Combinations Associated With Six Individual Sectors^a

	Waskesiu				Thompson			
	R	N_{hs}	%	Source Combination	R	N_{hs}	%	Source Combination
1999					0.967	3721	40.0	Sask, Man, Alb
1998	0.716	5975	32.4	Sask, Alb	0.884	2530	13.7	Man
1997	0.495	25	1.9	Sask	0.864	606	45.5	Man
1996	0.803	2820	57.1	Sask, NWT	0.82	234	4.7	Sask, Alb
1995	0.743	21315	52.3	NWT, Alb	0.894	40763	100.0	Sask, NWT, Yuk, Nun
1994	0.942	13523	33.5	Mani, Yuk, Nun	0.724	731	1.8	Nun

^aSee Figure 3 for a map. The R values are computed for the nine temporal bins (10-day composite data) straddling the June, July, and August period. Sask, Saskatchewan; Alb, Alberta; NWT, Northwest Territories; Yuk, Yukon; Man, Manitoba; Nun, Nunavut; N_{hs} is number of hot spots associated with the maximum correlation coefficient; % refers to number of hot spots for the most significant combination of the given year relative to the total number of hot spots for that year.

[28] The result is also supported indirectly by *Westphal and Toon* [1991] who pieced together a graph of (classical) Angstrom exponent versus smoke age to demonstrate a decreasing tendency. The equivalence between a trend versus smoke age and a trend versus optical depth is justifiable if one presumes that a significant proportion of τ_a changes are due to the increasing size of aging particles (as opposed to an influx of similarly sized particles). Figure 1b shows how variations in slope can occur; the slope $d\alpha_f/\log_{10}\tau_a$ changes from a minimum of ~ -1 for pure particle growth (case of $\langle\gamma\rangle = 0$) to values that progressively approach zero as the effects of particle influx become more important than particle growth. The three examples are governed by realistic rates of particle growth, abundance to particle growth rate (γ), and by the assumption that the particle growth rate varies as the number density or abundance [*Reid et al.*, 1998, 1999]). The values of the slope obtained encompass the slope values

(relative to α_f) in Table 2 and as such lend illustrative support to a general trend involving fine particle growth in the presence of differing degrees of abundance increase.

4. Focus on Smoke Events During the First Two Weeks of August 1998

[29] Figure 7 shows the six Sun photometer stations whose data were employed in this portion of the study as well as important forest fire sources that were active during the first two weeks of August 1998. The location and qualitative strength of these sources were identified from AVHRR imagery using algorithms for detecting fire hot spots [*Li et al.*, 2000] and smoke plumes [*Li et al.*, 2001]. A local fire which does not appear on this map but which probably had local effects on the Sun photometry of the Waskesiu station and which could be seen in the AVHRR

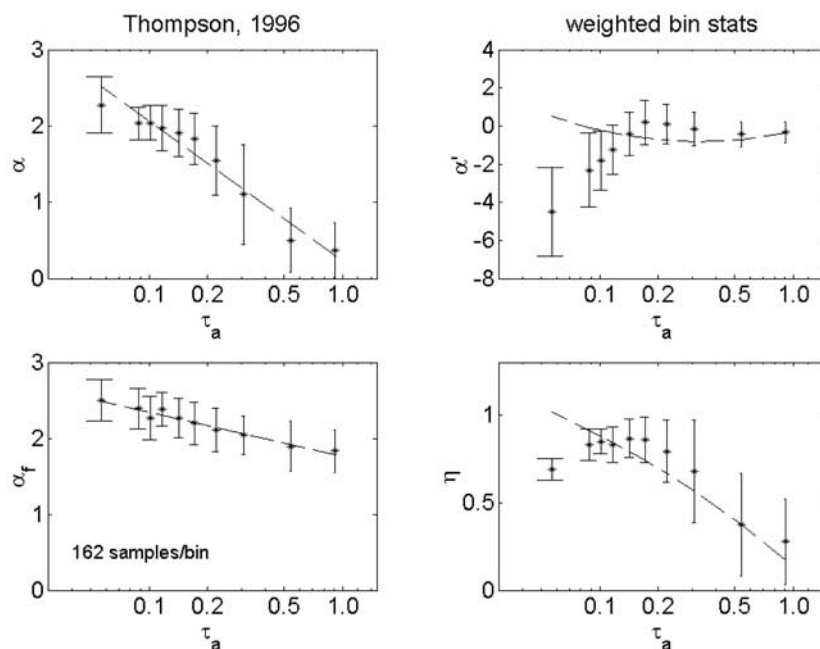


Figure 4. An illustration of the five standard optical parameters for the case of Thompson 1996. The error bars are estimates of standard deviation for the 10 equimeasurement bins across which the statistics were computed. The dashed lines for α and α_f are weighted linear fits, while the dashed line for η is the ratio (α/α_f) of these linear fits.

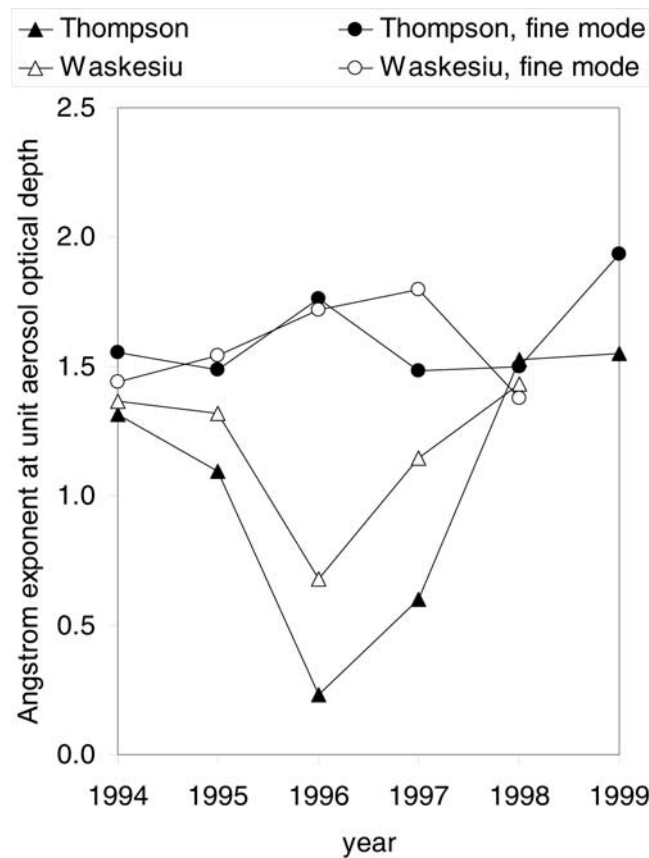


Figure 5. Total and fine mode Angstrom exponents, at $\tau_a = 1.0$, versus year for Thompson and Waskesiu ($\lambda = 500$ nm, cloud-screened and error-weighted data). These four curves correspond to the four columns of the regression parameter “ b ” in Table 2 (under “ α ” and “ α_f ” for Thompson and Waskesiu, respectively).

imagery occurred near Crean Lake about 30 km north of the Waskesiu site (P. Pacholek, personal communication, 2000).

[30] Table 3 is a compilation of smoke events seen by the Sun photometers at the different stations and referenced to the probable source of the smoke. The source column is a three-digit code for the fire source whose geographic location can be seen in Figure 7. Column 4 (D) is an estimate of the distance between a source fire and the Sun photometer station. Column 5 (Δt) is the approximate temporal range of the smoke event at a given station, while the following columns give the optical statistics (means and standard deviations). Columns 17 (r_{eff}) and 18 (ω_0) (single-scattering albedo) are averages of inversion data. Generally, only one to a few values of r_{eff} and ω_0 were available during the time period Δt (in particular for ω_0 , which requires rather large optical depths to achieve reasonable error levels [Dubovik *et al.*, 2000]).

[31] In order that a particular sequence of Sun photometer measurements be declared a smoke event, a number of criteria had to be satisfied. The back trajectory analyses had to indicate that the trajectory path at one or more of four pressure levels passed over the smoke sources indicated in Figure 7 and that the source was active at the corresponding time. All sequences declared to be smoke events were normally supported by TOMS imagery. AVHRR imagery and Meteosat imagery were used to support TOMS imagery and, on certain occasions (Bondville, Illinois, and Crean

Lake, Saskatchewan), were the only imagery available for a smoke event. The smoke discrimination criteria defined in Appendix C were used to check that the (noncloud screened) data defined as smoke was contained within certain bounded regions of α versus τ_a and $d\alpha/d\tau_a$ versus τ_a .

[32] Figure 8 shows the temporal variation of the hot spot count as well as $\tau_{a,g}$ and μ_τ for the summer of 1998 (the sampling in this case is over 10-day composites). The sectorial sources for the hot spot numbers (Manitoba for Thompson and Saskatchewan and Alberta for Waskesiu) were deduced from the best correlation coefficients (compare Table 1). The 2-week period that we employed to focus on smoke events at our six stations is shown between the dotted lines.

[33] Figure 9 shows an interesting example of the data sources brought to bear to identify a smoke event. In this particular case, smoke plumes from forest fires near Slave Lake, Alberta, traveled south on August 10 and then, according to the back trajectories, were transported west toward Waskesiu on August 11. Figure 10 shows the back trajectories referenced to the Waskesiu site along with TOMS imagery and AVHRR smoke-enhanced imagery. The plume effect is evident in both sets of imagery and is suggested in the peaking of the Sun photometer data around 11.7 UT. The fact that the more local sources of smoke are not seen in the TOMS imagery is consistent with the reported low-altitude aerosol insensitivity of this sensor.

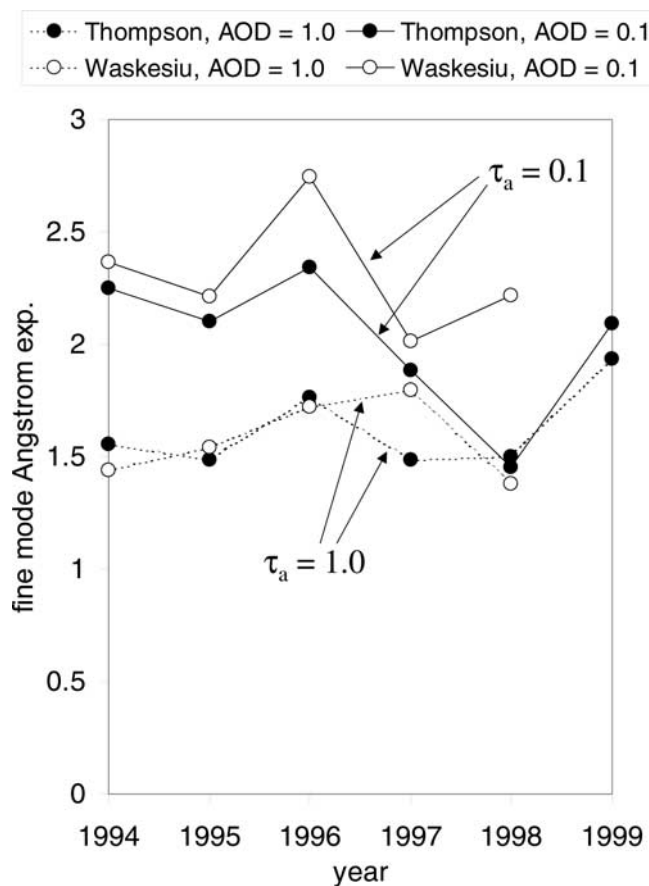


Figure 6. Fine mode Angstrom exponents (regressed to $\tau_a = 0.1$ and $\tau_a = 1.0$) versus year for Thompson and Waskesiu ($\lambda = 500$ nm, cloud-screened and error-weighted data). These curves correspond to the regression parameters “ c ” and “ b ” under the heading “ α_f ” in Table 2.

One can observe that the optical depths remain relatively large in the afternoon; this suggests, given the back trajectory analysis (not shown) and the AVHRR imagery, that the Crean Lake local source is the cause of the afternoon smoke event. The value of the α , which is systematically larger in the afternoon than in the morning, indicates the presence of

smaller aerosol particles in the afternoon and, from a pure standpoint of the distance dependence discussed below, that the afternoon aerosol is of a local nature.

[34] Table 4 lists the α versus τ_a statistics for all Sun photometer smoke events clumped indiscriminantly together. In spite of the geographic disparity of the sites

Table 2. Yearly Regression Statistics of α and α_f Versus τ_a and the Mean and Standard Deviation of η

	N_{bin}	α				α_f				η	
		a	b	c	$\sigma(\alpha)$	a	b	c	$\sigma(\alpha_f)$	$\langle\eta\rangle$	$\sigma(\eta)$
<i>Thompson</i>											
1994	121	0.04	1.44	1.39	0.10	-0.6	1.6	2.2	0.06	0.76	0.09
1995	84	-0.4	1.1	1.5	0.15	-0.44	1.65	2.09	0.10	0.77	0.04
1996	162	-1.8	0.3	2.1	0.17	-0.89	1.82	2.71	0.04	0.61	0.16
1997	76	-1.1	0.6	1.7	0.18	-0.35	1.81	2.16	0.04	0.85	0.06
1998	86	-0.2	1.5	1.7	0.04	-0.04	1.51	1.55	0.06	1.02	0.05
1999	54	-0.2	1.5	1.8	0.17	-0.34	1.92	2.27	0.10	0.80	0.04
<i>Waskesiu</i>											
1994	139	0.0	1.37	1.37	0.09	-0.9	1.44	2.366	0.09	0.69	0.1
1995	124	-0.3	1.32	1.61	0.15	-0.49	1.59	2.08	0.05	0.84	0.06
1996	155	-1	0.77	1.81	0.2	-1.02	1.65	2.67	0.09	0.63	0.08
1997	153	-0.7	1.12	1.79	0.11	-0.3	2.23	2.523	0.06	0.72	0.04
1998	172	-0.5	1.36	1.83	0.04	-0.73	1.70	2.42	0.03	0.8	0.04

(1) N_{bin} = number of data points per sampling bin. There were 10 sampling bins per α versus τ_a curve (compare Figure 4). (2) $\alpha = a \log_{10}(\tau_a) + b$ and therefore $a = d\alpha_f / \log\tau_a$, $b = \alpha(1.0)$, $c = b - a = \alpha(0.1)$, $\sigma(\alpha)$ is the standard deviation from the linear regression. The same regression parameter notation is used for α_f . (3) $\langle\eta\rangle$ and $\sigma(\eta)$ are the mean and standard deviation across the ten τ_a sampling bins (compare Figure 4).

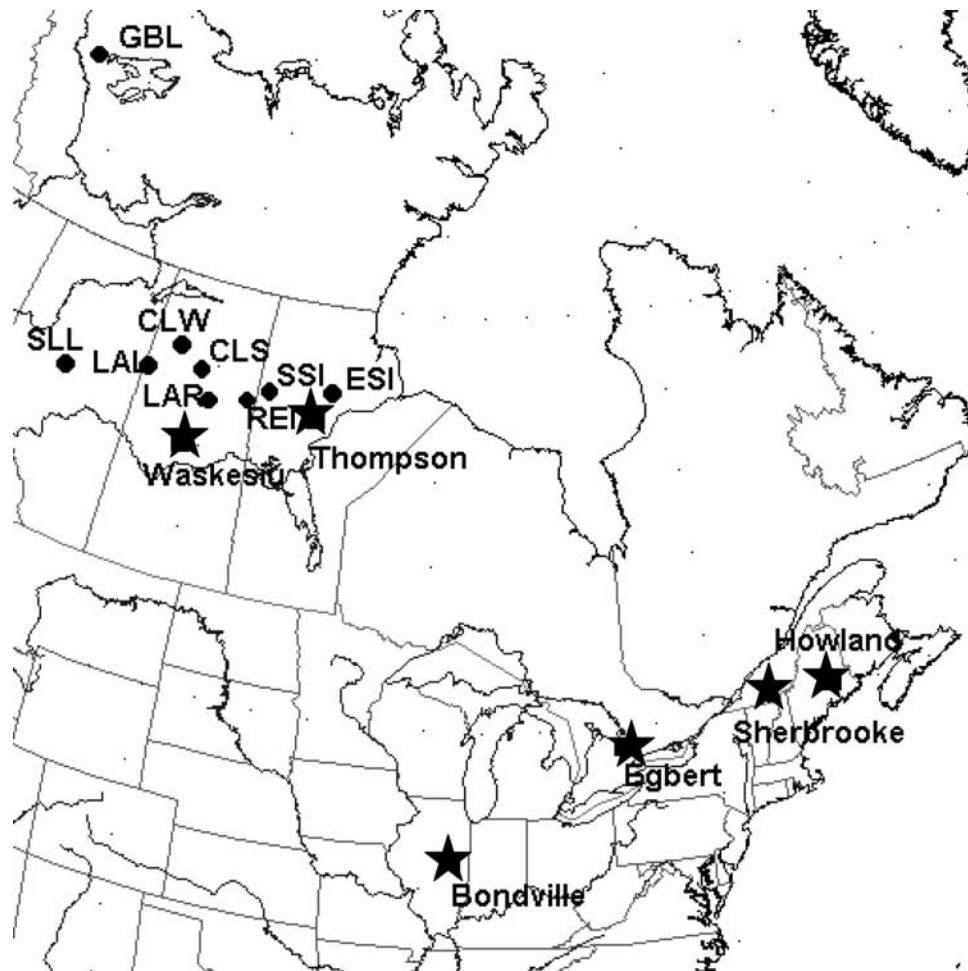


Figure 7. Major forest fire sources during the 2-week smoke events of 1998 (circles) and Sun photometer stations where smoke data were acquired. The codes for the major forest fire sources are given in Table 3.

relative to the sources, some resemblance between these latter graphs and the summer statistics of Thompson and Waskesiu is evident. A trend of decreasing α_f with τ_a similar to the trends typified by Figure 4 and the results of Table 2 yielded a value of $d\alpha_f/\log_{10}\tau_a \cong -0.5$ and a value of $\langle \gamma \rangle$ near 3 ($\langle d \log A/dr_{\text{eff}} \rangle$ of equation (B5). In this case, however, η was close to unity across the range of τ_a since the points had been carefully selected to represent fine particle smoke optical depths (in Table 4, the average across the 10 τ_a bins was $\langle \eta \rangle = 0.99$). An estimate of the corresponding change in r_{eff} , assuming an average of the smoke curves in Figure 1a, is roughly 0.10 to 0.15 μm (where the uncertainty associated with the range of all the smoke curves is about $\pm 0.01 \mu\text{m}$).

[35] Figure 11a shows plots of the decrease in average fine mode Angstrom exponent versus distance from the forest fire source and Figure 11b the increase in r_{eff} versus distance. The latter parameter was derived from radius averages applied to the fine mode component of the size distributions retrieved from solar and sky radiance inversions [Dubovik and King, 2000]. For Figure 11a we note a decrease in the dashed regression line from about 1.9 at 30 km to 1.4 at 2000 km. The regression line through the inversion results yields an increase in r_{eff} from about 0.13 to 0.15 μm between

30 and 2000 km. The associated estimates using averages of the smoke curves in Figure 1a are again roughly 0.10 to 0.15; the differences are in part due to the more comprehensive computations involved in the inversion procedure but are also very likely related to the relatively small number of points involved in the inversions).

[36] An analysis of mechanisms which might induce the trend toward larger particle size with increasing distance requires caution, given the disparity of sources and the complexity of smoke dispersion over thousands of kilometers. However, the trend is systematic and has similarities with the observations made above concerning the decreasing trends in α_f . In particular, the results are coherent with the observations of Westphal and Toon [1991], Kaufman *et al.* [1998], and Lioussé *et al.* [1995] concerning the decrease of the Angstrom exponent with smoke aging and those of Reid *et al.* [1998] who demonstrated an increase of smoke particle size with aging for Brazilian forest fire smoke.

[37] The back trajectories for the smoke events defined in Table 3 indicated that the travel times would vary from less than a day for the near-source cases to 4–5 days before the Great Bear Lake and Lower Lake, Athabasca, smoke plumes arrived at the eastern Sun photometer sites. In their analysis of Brazilian forest fire smoke, Reid *et al.*

Table 3. Parameters and Statistics for 1998 Smoke Events

Aug.	Station	Source	D , km	δt , UT	N	$\tau_{a,g}$	μ_{τ}	α	$\sigma(\alpha)$	α'	$\sigma(\alpha')$	α_f	$\sigma(\alpha_f)$	η	$\sigma(\eta)$	$r_{\text{eff},f}$	ω_0	Imagery Support ^a
<i>Nearby Sources: Crean Lake (Cobra)</i>																		
7	Wask	CRL	32	7.50–7.60	10	0.42	1.15	1.89	0.01	1.33	0.17	1.81	0.07	1.04	0.03	0.136	0.99	A
11	Wask	CRL	32	11.84–12.02	16	0.33	1.16	1.95	0.04	0.93	0.16	1.99	0.07	0.98	0.02	0.138	0.97	A
<i>Lower Lake Athabasca Fires</i>																		
9	<i>Wask^b</i>		<i>344</i>	<i>9.50–9.62</i>	<i>11</i>	<i>0.19</i>	<i>1.12</i>	<i>1.5</i>	<i>0.04</i>	<i>1.45</i>	<i>0.27</i>	<i>1.43</i>	<i>0.13</i>	<i>1.05</i>	<i>0.06</i>	<i>0.117</i>		<i>A, T</i>
10	Wask	CLS	306	10.55–11.00	40	0.23	1.18	1.83	0.08	0.68	0.38	1.97	0.12	0.94	0.07	0.137		A, T
12	Thom	CLS	516	12.81–12.91	10	0.95	1.3	1.2	0.12	0.86	0.33	1.4	0.09	0.89	0.1		0.85	T
<i>Slave Lake Fires</i>																		
11	Wask	SLL	606	11.55–11.64	12	0.3	1.23	1.65	0.02	1.08	0.1	1.68	0.04	0.98	0.02	0.14	0.98	A, T
12	Wask	SLL	606	12.91–13.05	13	0.6	1.28	1.7	0.1	1.48	0.18	1.59	0.14	1.07	0.04	0.17	0.99	T
<i>Distant Source: Great Bear Lake Fires</i>																		
4	Thom	GBL	1880	4.60–4.80	18	0.84	1.29	1.48	0.08	1.82	0.08	1.28	0.1	1.14	0.02	0.129	N/A	T
4	Thom	GBL	1880	4.9–5.05	14	0.43	1.16	1.62	0.09	1.9	0.1	1.32	0.07	1.14	0.03	0.156	0.92	T
8	Howl	GBL	4087	8.55–8.91	34	0.23	1.12	1.52	0.08	0.88	0.25	1.64	0.05	0.93	0.06	0.148		T
<i>Lower Lake Athabasca Fires</i>																		
11	Bond	CLS	2249	11.59–11.72	13	0.56	1.13	1.32	0.16	1.25	0.25	1.31	0.07	1	0.08	0.151	0.89	G
11	Bond	CLS	2249	11.77–11.9	13	1.06	1.06	1.3	1.01	1.94	0.03	1.06	0.01	1.2	0	0.136	0.93	G
12	Egbe	CLS	2299	12.46–12.60	20	0.26	1.48	1.3	0.15	2.01	0.47	1.25	0.25	1.07	0.1	0.18	0.73	T
13	Sher	CLS	2664	13.56–3.75	19	0.32	1.48	1.68	0.03	1.51	0.09	1.56	0.05	1.07	0.02	0.159	0.98	T
13	Sher	CLS	2664	13.75–13.96	25	0.38	1.26	1.39	0.21	2.17	0.34	1.41	0.18	1.09	0.05	0.164	0.96	T
<i>Salmon Arm, B.C.</i>																		
7	<i>Thom^b</i>		<i>1797</i>	<i>7.51–7.74</i>	<i>14</i>	<i>0.29</i>	<i>1.1</i>	<i>1.59</i>	<i>0.07</i>	<i>1.27</i>	<i>0.09</i>	<i>1.56</i>	<i>0.09</i>	<i>1.02</i>	<i>0.04</i>	<i>N/A</i>		<i>T</i>
7	<i>Thom^b</i>		<i>1797</i>	<i>7.74–8.01</i>	<i>14</i>	<i>0.66</i>	<i>2.01</i>	<i>1.47</i>	<i>0.19</i>	<i>1.59</i>	<i>0.73</i>	<i>1.51</i>	<i>0.17</i>	<i>1.01</i>	<i>0.16</i>	<i>1.43</i>	<i>0.9</i>	<i>T</i>

^aA, AVHRR; T, TOMS; G, GOES 10.

^bSalmon Arm and August 9 Waskesiu cases (in italic type) could not be satisfactorily linked to the Sun photometry on the basis of the smoke assessment criteria (these cases were not used in the statistical computations in the main text).

(ibidem) suggested that the principal mechanisms for the growth of regional smoke particles (1–4 days old) was condensation as well as particle coagulation and that after about 3 days of aging, coagulation would probably become the dominant mechanism. They also pointed out that condensation was more likely associated with high volatility organic species than water vapor since the influence of the latter was demonstrated to be weak [Kotchenruther and Hobbs, 1998]. A significant proportion of the condensation-induced particle growth was ascribed to cloud processing. Kaufman *et al.* [1998] pointed out that the size distribution of Brazilian smoke particles was fairly stable after about 3 days of aging; Remer *et al.* [1998] exploited this fact by employing optical depth measurements as a means of estimating cloud condensation nuclei (i.e., by assuming that changes in optical depths were mostly due to changes in number of smoke particles rather than size).

5. Conclusions

[38] Aerosol optical statistics for two western Canadian Sun photometer stations were analyzed for summertime data acquired between 1994 and 1999. It was demonstrated that a significant correlation exists with forest fire frequency indices (hot spots). This correlation indicates that on average, 80% of summertime optical depth variation in western Canada can be linked to forest fire sources.

[39] The average values of the geometric mean and standard deviation of $\tau_a(500 \text{ nm})$ was found to be 0.074

and 1.7, respectively, for the clearest, relatively smoke free year of 1997, while the values for the heaviest smoke year of 1995 were 0.23 and 3.0, respectively. The average (linear scale) modal value for the clearest year of 1997 was near 0.06.

[40] A new spectral technique for estimating the fine-particle Angstrom exponent (α_f) and the optical fraction of fine mode aerosols (η) was employed to extract the contributions of fine mode aerosols from the generic Angstrom exponent (α) and its spectral derivative (α'). This technique is particularly relevant to the isolation of fine mode smoke properties at small to moderate optical depths (at large distances from the forest fire source, for example) and in cases where homogeneous thin clouds contaminate the smoke optical depths. It could well be applied to the analysis of thin optical depth smoke in other regions such as South America and Africa where (as in the current study) spectral Sun photometry data are much more abundant than the combined Sun photometry and sky-scanning data employed to invert for particle size information.

[41] Systematic observations of decreasing α_f with increasing τ_a were noted; the average slope ($d\alpha_f/d \log \tau_a$) being of the order of -0.6 . This rate of decrease corresponds roughly to an abundance to particle size rate increase ($\langle \gamma \rangle = d \log A/d \log r_{\text{eff}}$) of ~ 2 and, in the absence of any a priori particle-type information, an increase in effective particle radius (r_{eff}) from about 0.09 to 0.15 μm .

[42] A 1998 series of forest fire events were tracked using TOMS, AVHRR, and GOES imagery, back trajectories, and

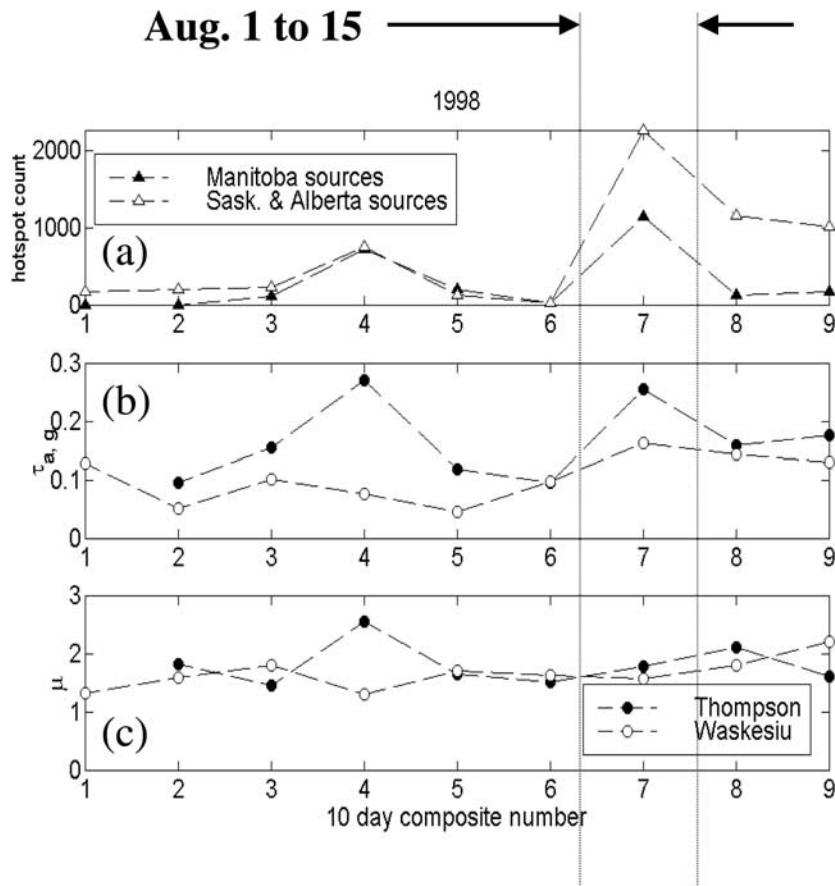


Figure 8. (a) Hot spot count for Manitoba sources (Thompson) and Saskatchewan and Alberta sources (Waskesiu) as a function of 10-day composite bin intervals over the summer months of June, July, and August 1998. (b, c) Geometric mean and geometric standard deviation for the Thompson and Waskesiu sites ($\lambda = 500$ nm; optical data are cloud screened and error weighted).

the optical depth data measured at six Sun photometer sites across Canada and the eastern United States. This data set provided a reference in terms of known smoke optical depths for the climatological statistics deduced for Thompson and Waskesiu. The results show similar rates of decrease of α_f with increasing τ_a : an average slope ~ -0.5 , an abundance to particle size rate increase ~ 3 , and a corresponding r_{eff} increase from approximately 0.10 to 0.15 μm . An analysis in terms of source to observation distance showed a decrease in α_f and an increase in r_{eff} with increasing source distance. This observation was coherent with previous studies on the particle growth effects of aging.

Appendix A: Data Processing Issues

A1. Data-Weighting Considerations

[43] In all averaging schemes involving the standard optical parameters (α , α' , α_f , and η), weights were assigned to a given parameter “ x ” according to the expression

$$\omega_x = \frac{\varepsilon_c^2}{\varepsilon_c^2 + \varepsilon_x^2}, \quad (\text{A1})$$

where ε_c is a threshold error and ε_x is the error in the parameter “ x ” associated with the quadrature sum of the

estimated instrumental error in τ_a plus the residual error between the third-order spectral polynomial in τ_a and the measured value of τ_a at 500 nm. One can appreciate the necessity for both terms of quadrature sum given that a perfect polynomial fit is no guarantee that the data are error free. The threshold error ε_c is needed to exclude inordinately large weights being assigned to τ_a spectra associated with spuriously small errors. The magnitude of ε_α and $\varepsilon_{\alpha'}$ were estimated using the expressions in the work of *O'Neill et al.* [2001b, equation (10)], while ε_{α_f} and ε_η were derived from differential relations related to ε_α and $\varepsilon_{\alpha'}$. It is noted also that in the case of α_f a damping weight was activated when the value of α_f exceeded the physical limits permitted for this parameter [*O'Neill et al.*, 2001a]. This situation often occurred when a particular band was known to be suspect.

A2. Relationship Between the Classical Angstrom Exponent and the Monochromatic Angstrom Exponent at 500 nm

[44] The classical Angstrom exponent (wavelengths 440, 500, 675, and 870 nm) is a standard of AERONET publications [e.g., *Holben et al.*, 2001], and thus it follows that the interrelationship with the monochromatic (500 nm) α defined above must be established. It

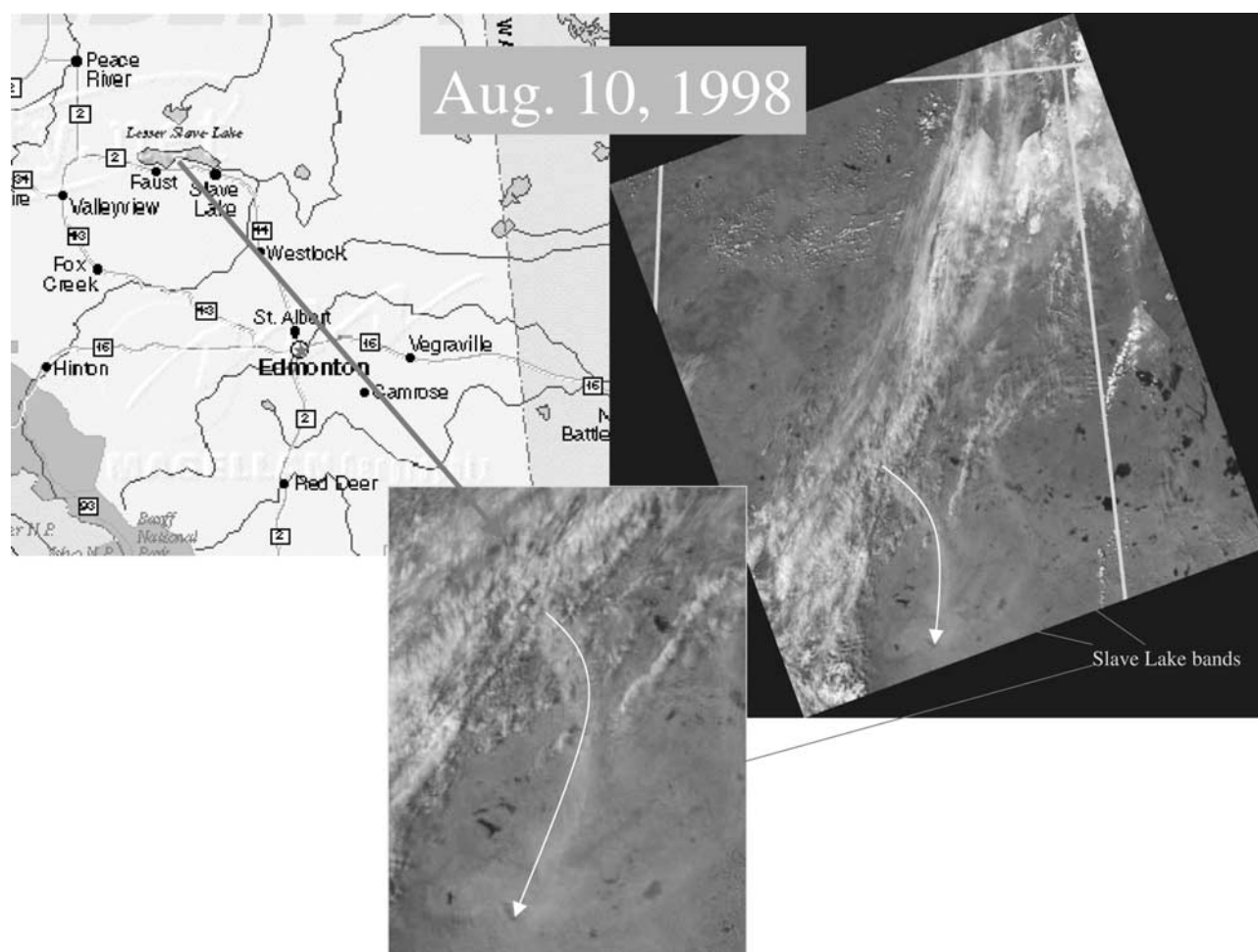


Figure 9. AVHRR smoke-enhanced data for the day preceding a smoke event at Waskesiu (10 August 1998). Bands of smoke from Slave Lake can be seen to be drifting south. See color version of this figure at back of this issue.

is noted that the AERONET Angstrom exponent is itself not a universal standard and that there are a variety of multiwavelength exponent regressions reported in the literature.

[45] The multiwavelength formulation of the AERONET exponent ($\alpha_{\text{classical}}$) suggests that it should be proportional to α and, in a second-order sense, to α' . Table A1 shows some regression results between $\alpha_{\text{classical}}$ and α for (1) Mie simulations over a variety of lognormal fine mode particle size distributions and a variety of refractive indices and (2) the Waskesiu and Thompson data ensemble defined in section 3 below. The exponent $\alpha_{\text{classical}}$ in the case of the fine mode Mie simulations is always greater than α since the Angstrom exponent typically increases with wavelength [Eck *et al.*, 1999], and thus a positive bias is necessary in the case of the zeroth-order expression of Table A1. In the case of the real Sun photometer data, one expects a variety of curvatures (a variety of α' values), and no strong bias exists or is expected if no discrimination in optical depth magnitude is made. If such regressions were tied to classes of optical depth magnitude there would be more of a tendency for a positive bias at large τ_a since an increase

in this parameter often coincides with an influx of fine mode particles.

Appendix B: Theoretical Expression for $d\alpha_f/d \log \tau_a$

[46] In the case of a pure fine mode aerosol component, one can express the aerosol optical variation in terms of the differential

$$d\tau_a = C_{\text{ext}} dA + A dC_{\text{ext}}, \quad (\text{B1})$$

where A is the abundance (aerosol particle number per cm^2 or μm^2 of atmospheric column), C_{ext} is the average extinction cross section in cm^2 or μm^2 of the total size distribution over altitude, and $\tau_a = AC_{\text{ext}}$. If we suppose that the rate of increase of r_{eff} is some function of A (linked by time in the case of diurnal events) then the differential $d\alpha_f$ can be normalized by the differential of $d \log \tau_a$ to yield the general derivative

$$\frac{d\alpha_f}{d \log \tau_a} = \frac{\frac{d\alpha_f}{d \log \tau_a}}{\frac{C_{\text{ext}}}{A} \frac{dA}{dC_{\text{ext}}} + 1} \quad (\text{B2})$$

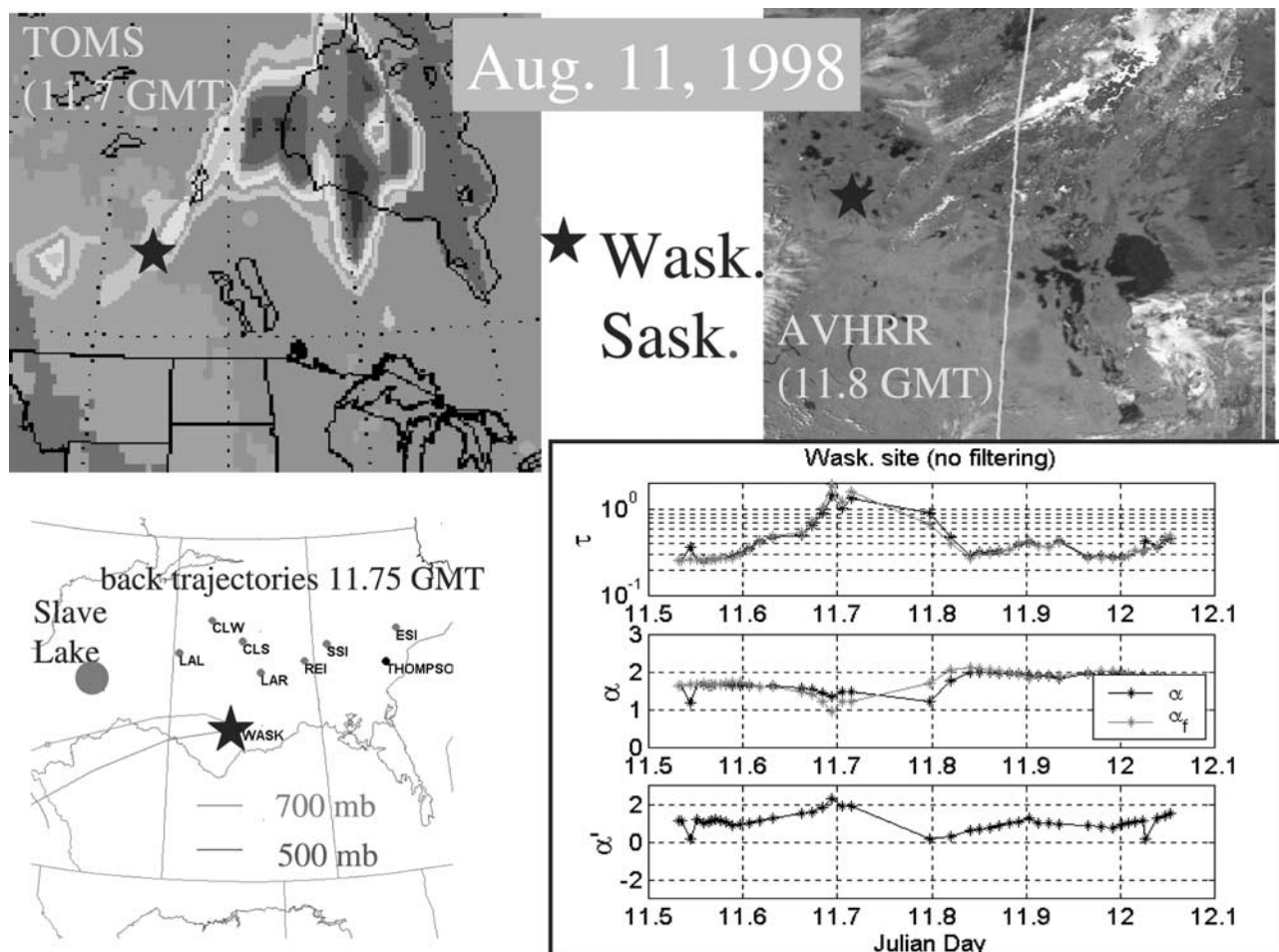


Figure 10. TOMS, AVHRR, back trajectory data, and Sun photometer data on 11 August 1998. The time unit is the day in August plus fractions of the day in UT. The TOMS equatorial crossing time is 1140 CST (1172 UT), while the AVHRR equatorial crossing time is 1430 CST (1185 UT). See color version of this figure at back of this issue.

relationship, where the logarithm is to the base 10 and where $\tau_a^* = A_0 C_{ext}$ is the increase in optical depth due to an increase in particle size only (due to an increase in C_{ext} only, with A fixed to some initial value A_0). Given that C_{ext} is positively correlated with r_{eff} , equation (B2) shows explicitly that for an increase in r_{eff} and a positive correlation between r_{eff} and A , the slope $d\alpha_f/d \log \tau_a^*$ is the maximum magnitude of $d\alpha_f/d \log \tau_a$. Equation (B2) can be further recast into a form that is more directly linked to variations in r_{eff} and A ;

$$\frac{d\alpha_f}{d \log \tau_a} = \frac{\frac{d\alpha_f}{d \log r_{eff}} \frac{1}{k}}{\frac{\gamma}{k} + 1}, \tag{B3}$$

$$\text{where } \gamma = \frac{d \log A}{d \log r_{eff}} = \frac{1/A}{1/r_{eff}} \frac{dA}{dr_{eff}},$$

and where we have used the approximation

$$\frac{d \log C_{ext}}{d \log r_{eff}} = \frac{(1/C_{ext})d C_{ext}}{(1/r_{eff})d r_{eff}} = k.$$

The parameter γ is a unitless variable representing the relative variation of the abundance A with respect to r_{eff} . The constant “ k ,” which describes the relative variation of

C_{ext} with respect to r_{eff} , is a typical empirical result for fits to Mie-scattering computations applied to lognormal size distributions. It is moderately dependent on the refractive index and the size distribution width of the aerosol which induces changes in the local optical depth. The form of the numerator in equation (B3) was inspired by previous studies, which indicated that α_f was approximately linear with $\log r_{eff}$ [e.g., O’Neill and Royer, 1993]. It is also moderately dependent on the refractive index and the size distribution width. It is noted that (as equation (B3) implies) the time element is not fundamental to the production of the curves in Figure 1b; what is important is how r_{eff} varies with A .

Table 4. Regression Statistics of α and α_f Versus τ_a and the Mean and Standard Deviation of η During the 2-week Period in August 1998^a

N_{bin}	All Stations									
	α				$7\alpha_f$				η	
	a	b	c	$\sigma(\alpha)$	a	b	c	$\sigma(\alpha_f)$	$\langle \eta \rangle$	$\sigma(\eta)$
15	-0.38	1.45	1.83	0.12	-0.48	1.45	1.93	0.08	0.99	0.08

^aAll smoke points from all stations are treated as one ensemble population. See footnotes of Table 2 for details.

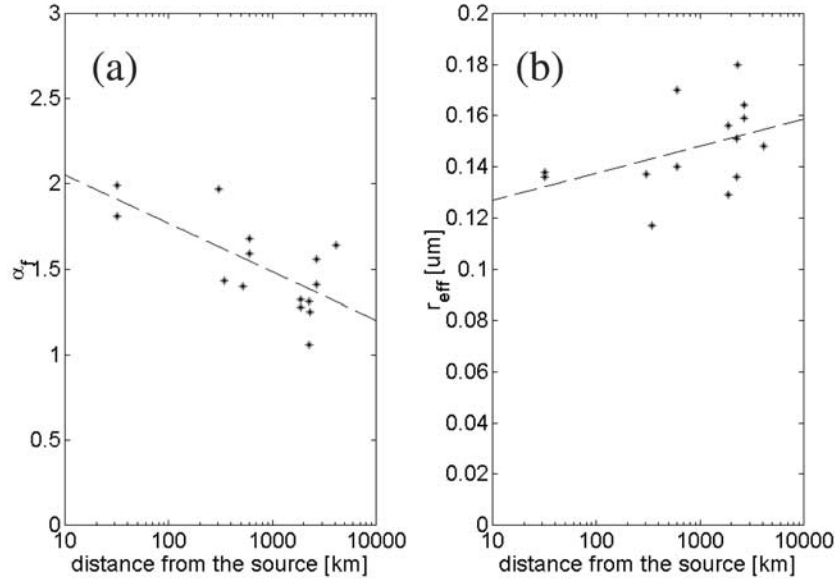


Figure 11. (a) α_f versus distance and (b) r_{eff} versus distance for the data of Table 3.

An approximation that is commensurate with regressions through the α_f versus $\log_{10}\tau_a$ curves is to work with averages (across τ_a) in equation (B3);

$$\left\langle \frac{d\alpha_f}{d\log\tau_a} \right\rangle \approx \frac{\frac{d\alpha_f}{d\log r_{\text{eff}}} \frac{1}{k}}{\frac{\langle \gamma \rangle}{k} + 1}, \quad (\text{B4})$$

so an estimate of the average rate of change of α_f versus $\log\tau_a$ can be used to infer the relative rate of change of abundance versus r_{eff} :

$$\langle \gamma \rangle \approx -3.3 \left\langle \frac{d\alpha_f}{d\log\tau_a} \right\rangle - 3.7, \quad (\text{B5})$$

where $d\alpha_f/d\log r_{\text{eff}}$ and k have been replaced by their nominal values for the smoke ($\mu_\tau = 1.5$) case of Figure 1a but where the deviations from $d\alpha_f/d\log r_{\text{eff}}$ and k are less than 15% and 25%, respectively, for all the cases shown in that figure.

[47] One final note is needed in order to apply these results to measured data. The equations above were developed for a single fine mode aerosol and so one should strictly plot α_f versus τ_f to analyze the interplay of fine mode number density and size effects. However, to minimize potential artifacts due to overprocessing and to maintain a standard τ_a axis (comparable to other work), we selected τ_a as the abscissa rather than τ_f . This is actually not a critical issue since the slope of α_f versus τ_f is close to the slope of α_f versus τ_f in the absence of large changes in η . Given that all variables are uniquely related as a function of time (that they are functions of each other), one can express the relationship between the two slopes, as below;

$$\begin{aligned} \frac{d\alpha_f}{d\log\tau_a} &= \frac{d\alpha_f}{d\log\tau_f} \frac{d\log\tau_f}{d\log\tau_a} \\ &= \frac{d\alpha_f}{d\log\tau_f} \left(\frac{d\log\eta}{d\log\tau_a} + 1 \right), \end{aligned}$$

which shows explicitly that the two slopes are identical if $\eta = \text{constant}$. A survey of our results indicated that changes in η (for τ_a between 0.1 and 1.0) rarely exceed the limits of 0.5 and 1.0 and were limited to a standard deviation range confined to values between 0.7 and 1.0. This yields equivalent logarithmic ranges of $\pm \log(1.4)$ and $\pm \log(1.2)$ and $d\log(\eta)/d\log\tau_a$ values of 30% and 16%, respectively.

Appendix C: Issues Related to Cloud Screening Versus Smoke Discrimination

[48] The transformation from α to α_f represents a form of cloud filtering in its own right. However, to address the issue of cloud screening versus smoke discrimination in the analysis of the August 1998 smoke events, we chose to work directly with α and in so doing to reduce the processing chain involved in cloud-screening/smoke-discriminating algorithm to a minimum. The results in this appendix represent a developmental effort at finding a smoke-discriminating algorithm based on simple physical concepts and built on the independently assessed 1998 smoke data.

Table A1. Expressions for $\alpha_{\text{classical}}$ and Associated RMS Errors^a

	0th Order in α'	RMS Error	1st Order in α'	RMS Error
Mie calculations ^b	$\alpha + 0.275$	0.081	$\alpha + 0.209 \alpha'$	0.038
Thompson and Waskesiu data ensemble ^c	α	0.23	$\alpha + 0.15 \alpha'$	0.17

^a $\alpha_{\text{classical}} = \alpha + k_0 + k_1 \alpha'$ where α and α' are evaluated at 500 nm.

^b Twenty-nine different lognormal size distributions of varying size parameters, real and complex refractive index [O'Neill et al., 2001a].

^c Average of (weighted) yearly regressions for all the multiyear data of section 3.

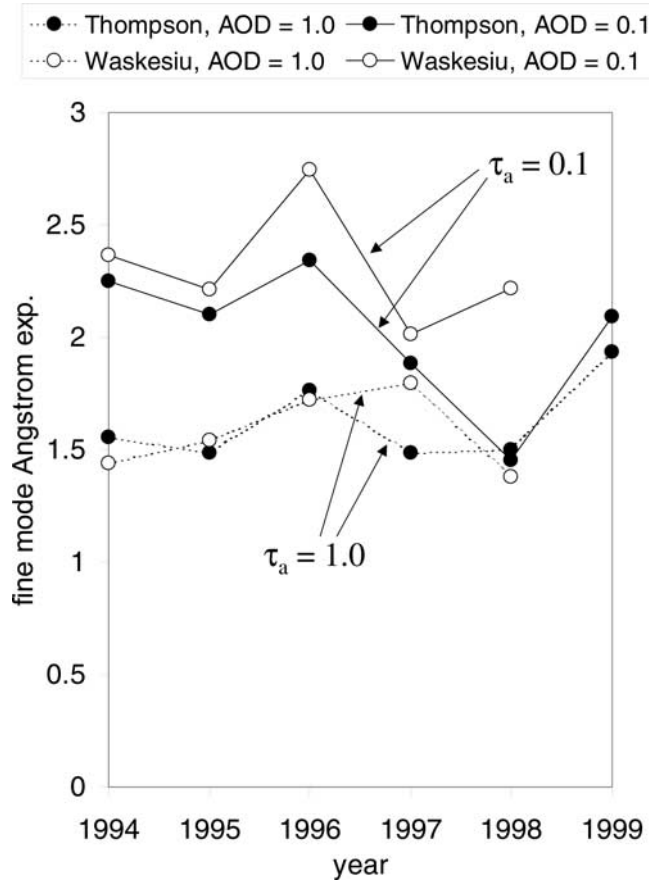


Figure A1. Sample of cloud discrimination criteria applied to data that have not been cloud screened according to the standard procedure (top pair of graphs) and which have been cloud screened using the standard procedure (bottom pair of graphs). The bounding conditions (solid lines) which define thin cloud conditions are given by $0.07 < \tau_a \alpha < 4.2$ on the α versus τ_a graphs and $-0.07 / \tau_a^2 > d\alpha/d\tau_a + \Delta(d\alpha/d\tau_a)$ and $d\alpha/d\tau_a - \Delta(d\alpha/d\tau_a) > -4.2 / \tau_a^2$ on the $d\alpha/d\tau_a$ versus τ_a graphs. The derivative $d\alpha/d\tau_a$ is computed from the ratio $[d\alpha/dt]/[d\tau_a/dt]$.

[49] Note that smoke discrimination is somewhat of a misnomer in that the real objective was to discriminate “noncloud” τ_a in order not to eliminate potential smoke data in any study of smoke statistics. The discrimination criteria, which are presented below, are confined to an appendix because they were not used in the climatological study of section 3 and because they were only used to check the veracity of the smoke label in section 4; they amount to a necessary condition for smoke but not a definition of smoke.

[50] Differentiating equation (1a) with respect to τ_a yields

$$\left(\frac{\partial\alpha}{\partial\tau_a}\right)_\lambda = (\alpha_f - \alpha_c) \left(\frac{\partial\eta}{\partial\tau_a}\right)_\lambda, \quad (C1)$$

where

$$\left(\frac{\partial\eta}{\partial\tau_a}\right)_\lambda = \frac{\xi}{\tau_a^2} \text{ where } \xi = \tau_c \left(\frac{\partial\tau_f}{\partial\tau_a}\right)_\lambda - \tau_f \left(\frac{\partial\tau_c}{\partial\tau_a}\right)_\lambda. \quad (C2)$$

In the presence of thin temporally variable cloud, τ_c is variable and τ_f is constant. Expressions (C1) and (C2)

accordingly reduce to

$$\frac{d\alpha}{d\tau_a} = \frac{-(\alpha_f - \alpha_c) \tau_f}{\tau_a^2}, \quad (C3)$$

where the partial derivative notation has been dropped for the sake of simplicity. Equation (1a) can be rewritten in a similar manner by eliminating τ_c ;

$$\alpha = \alpha_c + \frac{(\alpha_f - \alpha_c) \tau_f}{\tau_a} \approx \frac{(\alpha_f - \alpha_c) \tau_f}{\tau_a}, \quad (C4)$$

These expressions show analytically that we expect α to always decrease in the presence of a cloud-induced increase in τ_a . A range of values can be associated with the numerators of equations (C3) and (C4) and accordingly bounding expressions to identify thin cloud events can be defined. In addition to this essentially temporal criterion, one can impose a nontemporal criterion on α ; based on Mie computations such as those of Figure 1, we set this to be $\alpha < 1$ for cloud-contaminated optical depths.

[51] Figure A1 shows an example of these bounding expressions in α and $d\alpha/d\tau_a$ applied to all the data acquired

at Sherbrooke, Quebec, in the first two weeks of August 1998. The left-hand graphs show α versus τ_a , while the right-hand graphs show $d\alpha/d\tau_a$ versus τ_a . The upper pair of graphs are data which have not been cloud screened according to the standard procedure defined by Smirnov *et al.* [2000b], while the bottom pair is cloud screened. The upper bound in α (which is beyond the scale of the graph) and the lower bound in $d\alpha/d\tau_a$ are rather loosely defined according to whatever value of τ_f one chooses to define as a maximum.

[52] The circles represent data without restrictions, while the crosses represent values (including error bars) which fit into the cloud-bounding expression for $d\alpha/d\tau_a$. The solid grey circles represent data which were defined as a smoke event according to independent information (TOMs, back trajectories, etc.). One can note that the smoke event points are not defined as cloud (neither in terms of the α or the $d\alpha/d\tau_a$ criteria) and that a significant number of generic points are allowed into the $d\alpha/d\tau_a$ cloud zone because their error bars extend outside of the cloud boundaries. The standard cloud-screening algorithm does a good job of removing the cross-marked points and points for which $\alpha < 1$ but also removes points that have not been labeled as cloud for $\alpha > 1$.

[53] For the 2-week period of August 1998 and all six stations, standard cloud screening eliminated an average of about 48% of data for which $\alpha > 1$. An average of about 10% of unscreened data points with $\alpha > 1$ are actually eliminated by the derivative criterion on $d\alpha/d\tau_a$. If we accept the derivative criterion as a valid indicator of the noncloud label then about 38% of the points eliminated by the standard cloud-screening algorithm for $\alpha > 1$ should not have been eliminated since they may represent smoke.

[54] Thus the standard cloud-screening algorithm, which includes no spectral filtering criteria, largely succeeds in eliminating thin cloud based on temporal criteria only. It does, however, tend to overeliminate temporally variable data whose spectral behavior suggests that fine mode aerosols (and not coarse mode clouds) are the cause of the variation.

Notation

A	abundance (number of particles in an atmospheric column per unit area with typical units of cm^{-2} or μm^{-2}).
C_{ext}	average extinction cross section of a single aerosol particle (typical units of cm^2 or μm^2).
α_f	instantaneous slope of $-\ln \tau_f$ versus $\ln \lambda$.
α_c	instantaneous slope of $-\ln \tau_c$ versus $\ln \lambda$.
α	instantaneous slope of $-\ln \tau_a$ versus $\ln \lambda$; $\alpha = \alpha_f \eta + (1 - \eta)\alpha_c$.
α'_f	instantaneous slope of α_f versus $\ln \lambda$.
α'_c	instantaneous slope of α_c versus $\ln \lambda$.
α'	instantaneous slope of α versus $\ln \lambda$.
η	optical mixing ratio τ_f/τ_a .
γ	relative rate of increase of abundance with respect to r_{eff} (equation (B3)).
log	\log_{10} .
μ, μ_r, μ_τ	μ is the geometric standard deviation associated with a lognormal frequency distribution. If $\sigma(\log x)$ represents the standard deviation of a distribution of parameter x on a log scale then $\mu = 10^{\sigma(\log \cdot x)}$; μ_r and μ_τ are the explicit

representations of this parameter for a lognormal particle size distribution and a lognormal optical depth frequency distribution, respectively ($x = r$ and $x = \tau_a$); note that $\mu_r = \exp(\sigma_g)$ of Hansen and Travis [1974].

ω_0	Single-scattering albedo.
R	correlation coefficient for a linear regression.
r_{eff}	optically effective radius of a size distribution in μm ($= r_g \exp(2.5 \ln^2 \mu_r)$) for a lognormal size distribution, <i>ibidem</i>); in this paper, r_{eff} refers specifically to the fine mode (subscript "f" suppressed for simplicity).
r_g	geometric radius of a lognormal particle size distribution in μm (<i>ibidem</i>).
$\tau_{a,g}$	geometric mean of a frequency distribution of τ_a values.
τ_c	coarse mode optical depth.
τ_f	fine mode optical depth.
τ_a	total aerosol optical depth; $\tau_a = \tau_f + \tau_c$.

[55] Note that (1) all optical quantities are referenced to 500 nm wavelength and (2) parameters are unitless unless otherwise indicated.

[56] **Acknowledgments.** The authors would like to thank the National Research Council, NASA, the National Sciences and Engineering Research Council of Canada, and the Canadian Institute for Climate Studies for their financial support. Valuable in-kind support was obtained from the Canada Center for Remote Sensing (CCRS) and the Meteorological Services of Canada. The contributions of Ilya Slutsker of the AERONET group and Jin Ji-zhong of CCRS are particularly acknowledged.

References

- Allen, M., S. Raper, and J. Mitchell, Climate change—Uncertainty in the IPCC's third assessment report, *Science*, 293(5529), 430, 2001.
- Angstrom, A., On the atmospheric transmission of Sun radiation and on dust in the air, *Geogr. Ann.*, 11, 156–166, 1929.
- Chung, Y.-S., On the forest fires and the analysis of air quality data and total atmospheric ozone, *Atmos. Environ.*, 18(10), 2153–2157, 1984.
- Chung, Y.-S., and H. V. Le, Detection of forest-fire smoke plumes by satellite imagery, *Atmos. Environ.*, 18(10), 2143–2151, 1984.
- Dubovik, O., and M. D. King, A flexible inversion algorithm for retrieval of aerosol optical properties from Sun and sky radiance measurements, *J. Geophys. Res.*, 105, 20,673–20,696, 2000.
- Dubovik, O., B. N. Holben, Y. J. Kaufman, M. Yamasoe, A. Smirnov, D. Tanre, and I. Slutsker, Single-scattering albedo of smoke retrieved from the sky radiance and solar transmittance measured from ground, *J. Geophys. Res.*, 103, 31,903–31,924, 1998.
- Dubovik, O., A. Smirnov, B. N. Holben, M. D. King, Y. J. Kaufman, T. F. Eck, and I. Slutsker, Accuracy assessments of aerosol optical properties retrieved from AERONET Sun and sky-radiance measurements, *J. Geophys. Res.*, 105, 9791–9806, 2000.
- Dwyer, E., J.-M. Gregoire, and J.-P. Malingreau, A global analysis of vegetation fires using satellite images: Spatial and temporal dynamics, *Ambio*, 27, 175–181, 1998.
- Echalar, F., P. Artaxo, J. Vanderlei Martins, M. Yamasoe, F. Gerab, W. Maenhaut, and B. Holben, Long-term monitoring of atmospheric aerosols in the Amazon Basin: Source identification and apportionment, *J. Geophys. Res.*, 103, 31,849–31,864, 1998.
- Eck, T. F., B. N. Holben, J. S. Reid, O. Dubovik, A. Smirnov, N. T. O'Neill, I. Slutsker, and S. Kinne, The wavelength dependence of the optical depth of biomass burning, urban and desert dust aerosols, *J. Geophys. Res.*, 104, 31,333–31,350, 1999.
- Eck, T. F., B. N. Holben, D. E. Ward, O. Dubovik, J. S. Reid, A. Smirnov, M. M. Mukelabai, N. C. Hsu, N. T. O'Neill, and I. Slutsker, Characterization of biomass burning aerosols during the 1997 ZIBBEE Field Campaign, *J. Geophys. Res.*, 106, 3425–3448, 2001.
- Fedosejevs, G., N. T. O'Neill, A. Royer, P. M. Teillet, A. I. Bokoye, and B. McArthur, Aerosol optical depth for atmospheric correction of AVHRR composite data, *Can. J. Remote Sens.*, 26(4), 273–284, 2000.

- Ferrare, R. A., R. Fraser, and Y. J. Kaufman, Satellite measurements of large-scale air pollution: Measurements of forest fire smoke, *J. Geophys. Res.*, *95*, 9911–9925, 1990.
- Forgan, B. W., E. N. Rusina, J. J. Deluisi, B. B. Hicks, Measurements of atmospheric turbidity in BAPMON, and looking forward to GAW, *WMO Rep.* (draft 4), 80 pp., Geneva, Switzerland, 1993.
- Fraser, R., Z. Li, and J. Cihlar, Hotspot and NDVI differencing synergy (HANDS): A new technique for burned area mapping over boreal forest, *Remote Sens. Environ.*, *74*, 362–375, 2000.
- Freund, J., Aerosol optical depth in the Canadian Arctic, *Atmos. Ocean*, *21*(2), 158–167, 1983.
- Fromm, M., J. Alfred, K. Hoppel, J. Hornstein, R. Bevilacqua, E. Shettle, R. Servranckx, Z. Li, and B. Stocks, Observations of boreal forest fire smoke in the stratosphere by POAM III, SAGE II and lidar in 1998, *Geophys. Res. Lett.*, *27*(9), 1407–1410, 2000.
- Gueymard, C. A., Analysis of monthly average atmospheric precipitable water and turbidities in Canada and northern United States, *Solar Energy*, *53*(1), 57–71, 1994.
- Gueymard, C. A., and J. D. Garrison, Critical evaluation of precipitable water and atmospheric turbidity in Canada using measured hourly solar irradiance, *Solar Energy*, *62*(4), 291–307, 1998.
- Hansen, J. E., and L. D. Travis, Light scattering in planetary atmospheres, *Space Sci. Rev.*, *16*, 527–610, 1974.
- Hallett, J., J. G. Hudson, and C. F. Rogers, Characterization of combustion aerosols for haze and cloud formation, *Aerosol Sci. Technol.*, *10*, 10–83, 1989.
- Hariss, R. C., G. W. Sachse, G. H. Hill, L. Wade, K. G. Bartlett, J. E. Collins, L. P. Steele, and P. C. Novelli, Carbon monoxide and methane in the North American Arctic and subarctic troposphere, July–August 1988, *J. Geophys. Res.*, *97*, 16,589–16,599, 1992.
- Hobbs, P. V., J. S. Reid, J. A. Herring, J. D. Nance, R. E. Weiss, J. L. Ross, D. A. Hegg, R. D. Ottmar, and C. Liou, Particle and trace gas measurements in the smoke from prescribed burns of forest products in the Pacific Northwest, in *Biomass Burning and Global Change*, edited by J. S. Levine, pp. 697–715, MIT Press, Cambridge, Mass., 1996.
- Holben, B. N., A. Setzer, T. F. Eck, A. Pereira, and I. Slutsker, Effect of dry-season biomass burning on Amazon Basin aerosol concentrations and optical properties, 1992–1994, *J. Geophys. Res.*, *101*, 19,465–19,481, 1996.
- Holben, B. N., et al., AERONET—A federated instrument network and data archive for aerosol characterization, *Remote Sens. Environ.*, *66*, 1–16, 1998.
- Holben, B. N., et al., An emerging ground-based aerosol climatology: Aerosol optical depth from AERONET, *J. Geophys. Res.*, *106*, 12,067–12,097, 2001.
- Houghton, J. T., et al., (Eds.), *Climate Change 2001: The Scientific Basis*, pp. 896, Cambridge Univ. Press, New York, 2001.
- Hsu, N. C., J. R. Herman, J. F. Gleason, O. Torres, and C. J. Seftor, Satellite detection of smoke aerosols over a snow/ice surface by TOMS, *Geophys. Res. Lett.*, *26*(8), 1165–1168, 1999.
- Kaufman, Y. J., and R. S. Fraser, Light extinction by aerosols during summer air pollution, *J. Clim. Appl. Meteorol.*, *22*, 1694–1706, 1983.
- Kaufman, Y. J., A. Setzer, D. Ward, D. Tanré, B. N. Holben, P. Menzel, M. C. Pereira, and R. Rasmussen, Biomass burning airborne and spaceborne experiment in the Amazonas (BASE-A), *J. Geophys. Res.*, *97*, 14,581–14,599, 1992.
- Kaufman, Y. J., et al., Smoke, Clouds, and Radiation—Brazil (SCAR-B) experiment, *J. Geophys. Res.*, *103*, 31,783–31,808, 1998.
- Kotchenruther, R., and P. V. Hobbs, Humidification factors of aerosols from biomass burning in Brazil, *J. Geophys. Res.*, *103*, 32,081–32,089, 1998.
- Li, Z., Influence of absorbing aerosols on the inference of solar surface radiation budget and cloud absorption, *J. Clim.*, *11*, 5–17, 1998.
- Li, Z., and L. Kou, Atmospheric direct radiative forcing by smoke aerosols determined from satellite and surface measurements, *Tellus, Ser. B*, *50*, 543–554, 1998.
- Li, Z., J. Cihlar, L. Moreau, F. Huang, and B. Lee, Monitoring fire activities in the boreal ecosystem, *J. Geophys. Res.*, *102*, 29,611–29,624, 1997.
- Li, Z., S. Nadon, and J. Cihlar, Satellite detection of Canadian boreal forest fires: Development and application of an algorithm, *Int. J. Remote Sens.*, *21*, 3057–3069, 2000.
- Li, Z., A. Khananian, R. Fraser, and J. Cihlar, Detecting smoke from boreal forest fires using neural network and threshold approaches applied to AVHRR imagery, *IEEE Trans. Geosci. Remote Sens.*, *39*, 1859–1870, 2001.
- Lioussé, C., C. Devaux, F. Dulac, and H. Cachier, Aging of savanna biomass burning aerosols: Consequences on their optical properties, *J. Atmos. Chem.*, *22*, 1–17, 1995.
- Markham, B. L., J. S. Schafer, B. N. Holben, and R. N. Halthore, Atmospheric aerosol and water vapor characteristics over north central Canada during BOREAS, *J. Geophys. Res.*, *102*, 29,737–29,745, 1997.
- Mazurek, M. A., W. A. Cofer, and J. S. Levine, Carbonaceous aerosols from prescribed burning of a boreal forest ecosystem, in *Global Biomass Burning: Atmospheric, Climatic, and Biospheric Implications*, edited by J. S. Levine, pp. 258–263, MIT Press, Cambridge, Mass., 1991.
- Miller, J. R., and N. T. O'Neill, Multialtitude airborne observations of the insolation effects of forest fire smoke aerosols at BOREAS: Estimates of aerosol optical parameters, *J. Geophys. Res.*, *102*, 29,729–29,736, 1997.
- O'Neill, N. T., and A. Royer, Extraction of bimodal aerosol size distribution from spectral and angular slope (Angstrom) coefficients, *Appl. Opt.*, *32*(9), 1642–1645, 1993.
- O'Neill, N. T., A. Ignatov, B. N. Holben, and T. F. Eck, The lognormal distribution as a reference for reporting aerosol optical depth statistics; empirical tests using multi-year, multi-site AERONET sunphotometer data, *Geophys. Res. Lett.*, *27*, 3333–3336, 2000.
- O'Neill, N. T., O. Dubovik, and T. F. Eck, A modified Angstrom exponent for the characterization of sub-micron aerosols, *Appl. Opt.*, *40*(15), 2368–2374, 2001.
- O'Neill, N. T., T. F. Eck, B. N. Holben, A. Smimov, and O. Dubovik, Bimodal size distribution influences on the variation of Angstrom derivatives in spectral and optical depth space, *J. Geophys. Res.*, *106*, 9787–9806, 2001.
- Patterson, E. M., and C. K. McMahon, Absorption characteristics of forest fire particulate matter, *Atmos. Environ.*, *18*, 2541–2551, 1984.
- Polavarapu, R. J., Atmospheric turbidity over Canada, *J. Appl. Meteorol.*, *17*, 1368–1374, 1978.
- Pueschel, R. F., and J. M. Livingston, Aerosol spectral optical depths: Jet fuel and forest fire smokes, *J. Geophys. Res.*, *95*(D123), 22,412–22,417, 1990.
- Pueschel, R. F., J. M. Livingston, P. B. Russell, D. A. Colburn, T. P. Ackerman, D. A. Allen, B. D. Zak, and W. Enfield, Smoke optical depths: Magnitude, variability, and wavelength dependence, *J. Geophys. Res.*, *93*, 8388–8402, 1988.
- Radke, L. F., Airborne observations of cloud microphysics modified by anthropogenic forcing, in *Symposium on Atmospheric Chemistry and Global Climate*, Am. Meteorol. Soc., Boston, Mass., 1989.
- Radke, L. F., J. L. Stith, D. A. Hegg, and P. V. Hobbs, Airborne studies of particles and gases from forest fires, *J. Air Pollut. Control Assoc.*, *28*, 30–34, 1978.
- Radke, L. F., D. A. Hegg, J. H. Lyons, C. A. Brock, P. V. Hobbs, R. Weiss, and R. Rasmussen, Airborne measurements on smokes from biomass burning, in *Aerosols and Climate*, edited by P. V. Hobbs and M. P. McCormick, pp. 411–422, A. Deepak, Hampton, Va., 1988.
- Radke, L. F., D. A. Hegg, P. V. Hobbs, J. D. Nance, J. E. Lyons, K. K. Laursen, R. E. Weiss, P. J. Riggan, and D. E. Ward, Particulate and trace gas emissions from large biomass fires in North America, in *Global Biomass Burning: Atmospheric, Climatic, and Biospheric Implications*, edited by J. S. Levine, pp. 209–224, MIT Press, Cambridge, Mass., 1991.
- Reid, J. S., and P. V. Hobbs, Physical and optical properties of young smoke from individual biomass fires in Brazil, *J. Geophys. Res.*, *103*, 32,013–32,031, 1998.
- Reid, J. S., P. V. Hobbs, R. J. Ferek, D. R. Blake, J. V. Martrins, M. R. Dunlap, and C. Lioussé, Physical, chemical, and optical properties of regional hazes dominated by smoke in Brazil, *J. Geophys. Res.*, *103*, 32,059–32,080, 1998.
- Reid, J. S., T. F. Eck, S. A. Christopher, P. V. Hobbs, and B. N. Holben, Use of the Angstrom exponent to estimate the variability of optical and physical properties of aging smoke particles in Brazil, *J. Geophys. Res.*, *22*, 27,473–27,489, 1999.
- Remer, L. A., Y. J. Kaufman, B. N. Holben, A. M. Thompson, and D. McNamara, Biomass burning aerosol size distribution and modeled optical properties, *J. Geophys. Res.*, *103*, 31,879–31,891, 1998.
- Remer, L., Y. J. Kaufman, and B. N. Holben, Interannual variation of ambient aerosol characteristics on the east coast of the United States, *J. Geophys. Res.*, *104*, 2223–2231, 1999.
- Robock, A., Enhancement of surface cooling due to forest fire smoke, *Science*, *24*, 911–913, 1988.
- Shifrin, K. S., Simple relationships for the Angstrom parameter of disperse systems, *Appl. Opt.*, *34*(21), 4480–4485, 1995.
- Smimov, A. V., A. Royer, N. T. O'Neill, and A. Tarussov, A study of the link between synoptical air mass and atmospheric optical parameters, *J. Geophys. Res.*, *99*, 20,967–20,982, 1994.
- Smimov, A. V., N. T. O'Neill, A. Royer, A. Tarussov, and B. McArthur, Aerosol optical depth over Canada and the link with synoptical air mass types, *J. Geophys. Res.*, *101*, 19,299–19,318, 1996.
- Smimov, A., B. N. Holben, O. Dubovik, N. T. O'Neill, and L. A. Remer, Measurements of atmospheric optical parameters on U.S. Atlantic coast sites, ships, and Bermuda during TARFOX, *J. Geophys. Res.*, *105*, 9887–9901, 2000a.

- Smirnov, A., B. N. Holben, T. F. Eck, O. Dubovik, and I. Slutsker, Cloud screening and quality control algorithms for the AERONET database, *Remote Sens. Environ.*, 73, 337–349, 2000b.
- Stocks, B. J., The extent and impact of forest fires in northern circumpolar countries, in *Global Biomass Burning: Atmospheric, Climatic, and Biospheric Implications*, edited by J. S. Levine, pp. 197–202, MIT Press, Cambridge, Mass., 1991.
- Uboegbulam, T. C., and J. A. Davies, Turbidity in eastern Canada, *J. Appl. Meteorol.*, 22, 1384–1492, 1983.
- Ward, D. E., A. W. Setzer, Y. J. Kaufman, and R. A. Rasmussen, Characteristics of smoke emissions from biomass fires of the Amazon region—BASE-A experiment, in *Global Biomass Burning: Atmospheric, Climatic, and Biospheric Implications*, edited by J. S. Levine, pp. 394–402, MIT Press, Cambridge, Mass., 1991.
- Westphal, D. L., and O. B. Toon, Simulations of microphysical radiative, and dynamical process in a continental-scale forest fire smoke plume, *J. Geophys. Res.*, 96, 22,379–22,400, 1991.
- Wong, J., and Z. Li, Retrieval of optical depth for heavy smoke aerosol plumes: Uncertainties and sensitivities to the optical properties, *J. Atmos. Sci.*, 59, 250–261, 2002.
- Woods, D. C., R. L. Chuan, W. R. Cofer III, and J. S. Levine, Aerosol characterization in smoke plumes from a wetlands fire, in *Global Biomass Burning: Atmospheric, Climatic, and Biospheric Implications*, edited by J. S. Levine, pp. 241–244, MIT Press, Cambridge, Mass., 1991.
- Wotawa, G., and M. Trainer, The influence of Canadian forest fires on pollutant concentrations in the United States, *Science*, 288, 324–328, 2000.
- Yamashita, S., A comparative study of turbidity in an urban and a rural environment at Toronto, *Atmos. Environ.*, 8, 507–518, 1974.
- Zhang, J., S. A. Christopher, and B. N. Holben, Intercomparison of smoke aerosol optical thickness derived from GOES 8 imager and ground-based Sun photometers, *J. Geophys. Res.*, 106, 7387–7397, 2001.

T. F. Eck, B. N. Holben, and A. Smirnov, NASA Goddard Space Flight Center, Greenbelt, MD 20771, USA.

Z. Li, Department of Meteorology, University of Maryland, College Park, MD 20742, USA.

N. T. O'Neill, and A. Royer, CARTEL, Université de Sherbrooke, 2500 Bd., Sherbrooke, Québec, Canada, J1K 2R1. (noneill@courrier.usherb.ca)

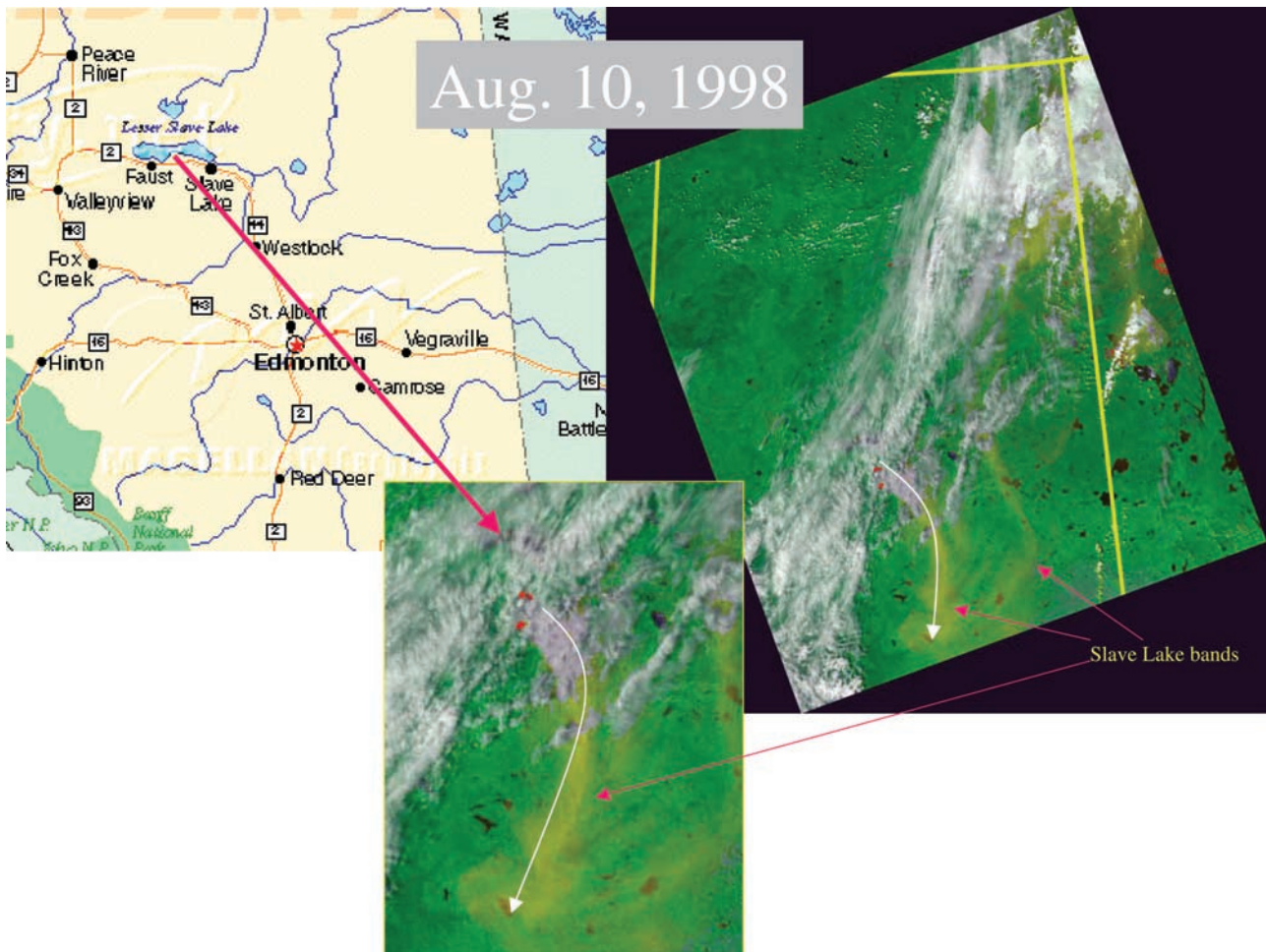


Figure 9. AVHRR smoke-enhanced data for the day preceding a smoke event at Waskesiu (10 August 1998). Bands of smoke from Slave Lake can be seen to be drifting south.

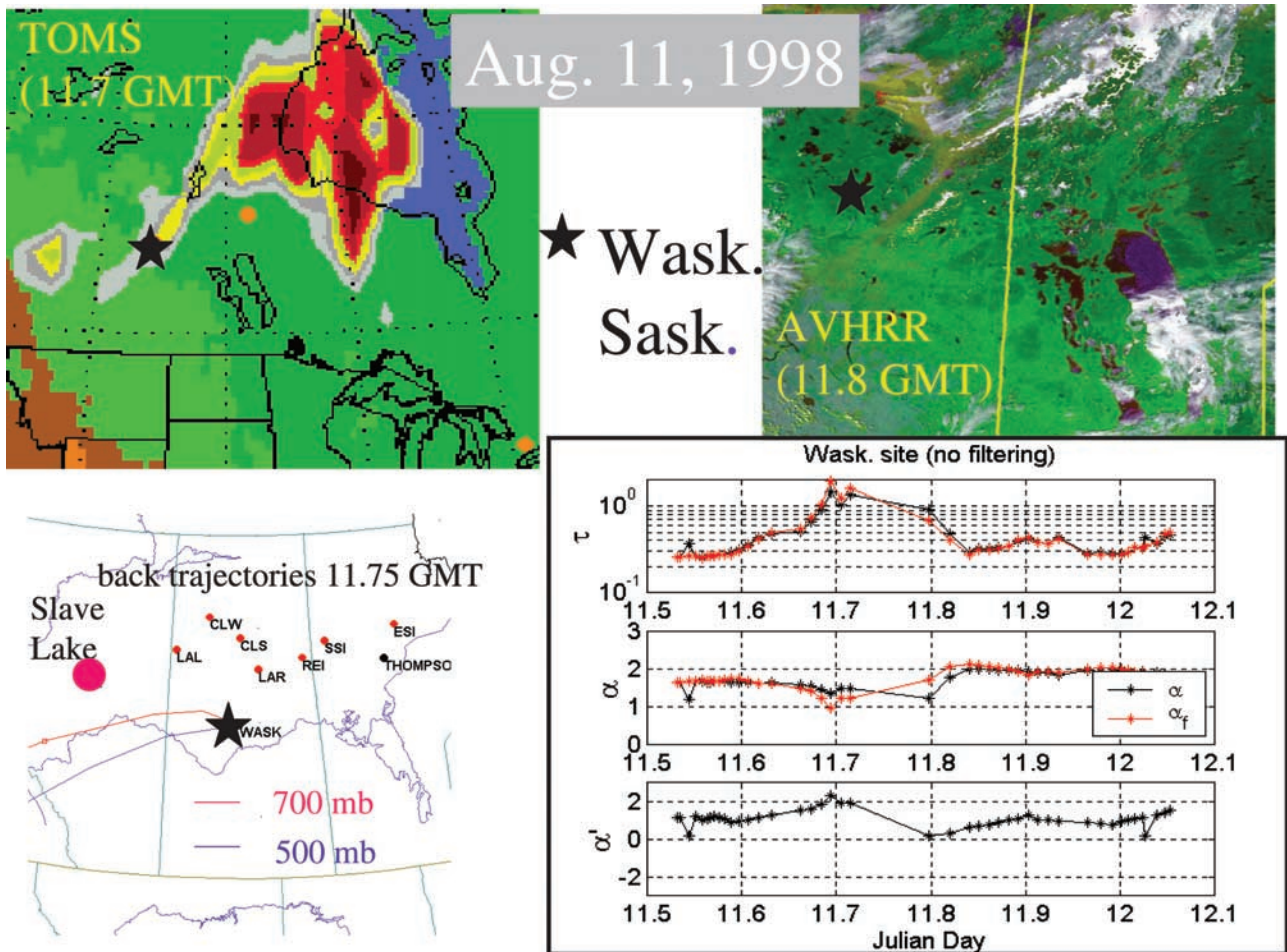


Figure 10. TOMS, AVHRR, back trajectory data, and Sun photometer data on 11 August 1998. The time unit is the day in August plus fractions of the day in UT. The TOMS equatorial crossing time is 1140 CST (1172 UT), while the AVHRR equatorial crossing time is 1430 CST (1185 UT).